POLITECNICO DI TORINO

Master of Science in Physics of Complex Systems

Master's degree Thesis

Tuning metallic and insulating phases of 2D transition metal dichalcogenides by ionic-gate induced intercalation of hydrogen and hydrogen-rich ions

Supervisors

Prof. Renato GONNELLI

Dr. Erik PIATTI

Candidate

Daria FERRARIS

December 2022

Abstract

This thesis project aimes at tuning the metallic and insulating phases of four transition metal dichalcogenides (TMDs) by means of gate-induced intercalation of hydrogen (H) or hydrogen-rich ions under optimised gating conditions. The gating technique induces an intense electric field at the interface between an electrolyte and the surface of the material under investigation. The ionic-gate-induced intercalation of H ions (protonation) entails or hydrogen-rich ions entails the hydrolysis (electrolysis) of the remaining water present in the solution in order to implant H^+ ions into the system by exploiting the ultra-high interface electric field. The gate-induced electric field can also result in the direct intercalation of the H-rich molecular cations composing the electrolyte. In this thesis work we focused on four selected materials: the transition metal dichalcogenides (TMDs) TaS_2, VSe_2, $NiTe_2$ and WSe_2. We apply on them the intercalation of hydrogen and hydrogen-rich ions to induce electron doping and possible structural modifications. This in turn allows to affect the ground state of these materials and to tune their structural and electronic properties, with a specific focus on the charge-density-wave phases (CDW).
Evident CDW behavior was observed in TaS_2 and VSe_2 pristine samples, showing the CDW phase transition at 230 K and 101 K, respectively. In TaS_2, the long gating time intercalation at the temperature T=350K was able to suppress the CDW and to obtain a transition from insulating to metallic behavior. Moreover, the intercalation effect on resistivity was found to be non-volatile, as it was monitored three weeks after the gating process and after an additional annealing at 350 K. VSe_2 showed CDW and metallic behavior. Intercalated samples presented highly increased resistivity with the transition from metallic to insulating behavior. This effect is attributed to VSe_2 exhibiting a nearly-compensated semimetallic bandstructure, where electron doping causes a transition from an electron-type metallic behavior to a hole-type insulating one. Also, the macroscopic effect of H-rich ions intercalated into the TMD layered structures was visible on the relevant growing of thickness after the gating process.
In WSe_2 and $NiTe_2$ samples, intercalation acted mainly as electron doping, increasing the level of conductivity along the whole T interval. It almost resulted in a resistivity curve with similar trend to the pristine sample, rescaled by a constant. The conductivity increase was related to gating time, due to higher intercalation level. In $NiTe_2$ the metallic behavior was enhanced, and at low T, the decrease in the residual resistivity ratio (RRR) indicated a possible reduction of the disorder in the intercalated structure. Differently, WSe_2 still maintained insulator behavior. The analysis of the logarithm of conductivity on the Arrhenius plot of WSe_2 showed

a Mott's variable range hopping (VRH) conductive regime at low T.
No samples presented the transition to the superconducting state. However, the effects observed on the behavior of the intercalated structures are promising. Further research can be devoted to the implementations of H intercalation by ionic-gating technique.

Acknowledgements

At the end of this thesis, I would like to thank professor Renato Gonnelli, doctor Erik Piatti, and professor Dario Daghero for the time and attention they have devoted to us students. Also, I thank for the opportunity to follow this project both for the stimuli and curiosity, and for the meaning and details of scientific research. Professor Renato Gonnelli, from the very first lessons in solid state physics, struck me with his passion and ability to communicate with us students. On the other hand Dr. Erik Piatti followed us in every stage of the thesis with his rigor and method.

Thanks to Jessica and Tohid for the support, it was a pleasure to share this thesis journey together.

Thanks to my parents, because they nourish me with their trust and their example of constant commitment and interest in life. To my mum Katia who always amazes me with an extra point of view. To my dad Stefano who always encourages me to give more. To my brother Guglielmo who is always present with his sensibility.

Finally, I want to deeply thank all the people who have taken me by hand during these years. It has been a journey of novelties and difficulties that has challenged me. They taught me to enjoy the complexity and to be ready to learn from everyone.

List of acronymes

AL Anderson Localisation
(AD)XRD (angle dispersive) X-ray diffraction
ARPES angle resolved photoemission spectroscopy
B magnetic field T
BSP Brillouin symmetry points
CALYPSO crystal structure analysis by particle swam optimization
CDW charge density waves
C-CDW commensurate charge density waves
CVD chemical vapor deposition
CVT chemical vapor transport
DC direct current
DFT density functional theory
DOS density of states
EDL electric double layer
E_F Fermi energy, eV
FeSe iron selenide
FL Fermi liquid
FS Fermi surface
FET field effect transistors
H hydrogen
H^+ hydrogen positive ion - proton
IC-CDW incommensurate charge density waves
iFET ionic field effect transistors
IR infrared spectroscopy
MoS_2 molybdenum disulfide
NC-CDW nearly commensurate charge density waves
$NiTe_2$ nickel ditelluride
NMR nuclear magnetic resonance
p pressure, Pa
OCV open circuit voltage
Pd palladium
PdCu palladium copper
QCP quantum critical point

R resistance, Ω
RRR residual resistance ratio
ρ resistivity, $\Omega/cdotcm$
RT room temperature, K
RTFM room temperature ferromagnetism
SC superconductors - superconductivity
SIC-FET solid ion conductor field effect transistor
SDW spin density waves
T temperature, K
TaS_2 tantalum disulfide
T_C critical temperature, K
T_D degenerate temperature, K
Th thorium
TMD transition metal dichalcogenides
vdW van der Waals (forces)
V_g gate voltage, V
VRH variable range hopping (regime)
VSe_2 vanadium diselenide
WSe_2 tungsten disulfide
XPS X-Ray photoelectron spectroscopy
XRD X-ray diffraction

1D mono-dimensional
2D bi-dimensional
3D tri-dimensional

Table of Contents

Chapter 1

Introduction, a novel ionic gating technique

The **superconductive (SC)** phase of a material is characterized by two main features affecting its behaviour: when reaching the SC phase the electrical resistivity (ρ) drops to zero and the magnetic-field flux ($\Phi(B)$) is ejected from the material (Meissner effect) (see Fig. 1.1).
Specifically, a superconductor has a characteristic **critical temperature** T_C below which its resistivity drops abruptly to zero and the material shows SC behaviour. On the contrary, a metallic conductor which does not exhibit SC behaviour shows a resistivity that gradually decreases with decreasing temperature (T) without a localized drop. The pressure (p) condition modifies the value of T_C that corresponds to the transition to SC phase in the material.

In the last decades, room-temperature (RT) superconductivity has been approached in some H intercalated materials, but only under very high pressures of approximately 200 GPa [2]. The employment of high pressures limits the applications of the discoveries, leading to the consideration of other methods for tuning the SC phase.

From a theoretical point of view the observation of SC behaviour on materials allowed to study the electron-phonon interaction that sustains the near-RT SC, and also to study the role of doping or other strategies in regulating the structural properties that favour large SC critical temperatures. Following on from these discoveries, the present work is part of the body of research which aims to obtain high-T superconductors under **ambient pressure conditions** [3].

The literature suggests that the SC phase can be induced in different materials, whether in ambient temperature and ambient pressure conditions their intrinsic

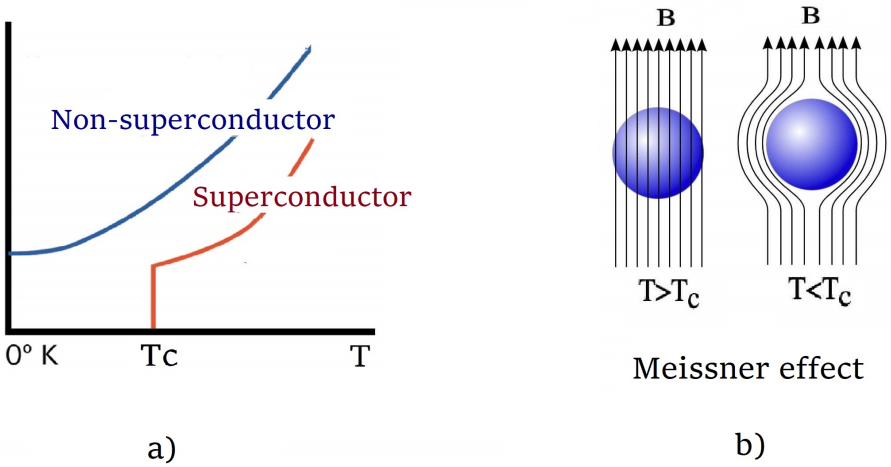

Figure 1.1: *The main features distinguishing a superconductor: (a) resistivity drop at T_C and (b) ejected magnetic-field flux (Meissner effect) [1].*

ground states are those of an insulator, a semiconductor or a metal. Several strategies can be used to this end, including applying pressure [4], different types of electron and hole doping [5] [6], intercalating a spacing layer [7] and reducing dimensionality [8].

In the present research work we focus on the **intercalation of H and H-rich organic ions** to tune the electronic properties of selected materials, aiming at establishing a platform to attain H-induced superconductivity at ambient pressure.

In the last 50 years [9], some first examples of H intercalation in palladium (Pd) demonstrated the induction of SC phase and the increase of T_C at $T_C = 9.4K$ and in thorium (Th) at $T_C = 8.2K$. Subsequently, this has been applied in different alloys. For many years H intercalation did not attract attention and research was focused on cuprates, a class of high-T_C SC materials, while at high pressures the highest T_C results were achieved in H_3S and LaH_{10}. On the contrary, in the last years the techniques based on the introduction of H and H-rich compounds have been successfully employed at ambient pressure. It is possible to cite [10] the example of protonated FeSe samples where $T_C \approx 45K$ was reached by using the ionic liquid gating method. Moreover, exploiting different techniques, relevant results have been obtained by the reduction of the dimensionality: signs of superconductivity with T_C above $65K$ have been observed in monolayers of $FeSe/SrTiO_3$.

As shown in the following paragraphs, the choice of materials for research has been oriented towards **layered transition metal dichalcogenides (TMDs)**. Several good results are reported for intercalated TMDs. An interesting example is the ion-gated MoS_2 surface doped with an electrostatic field [11]. Moreover, some hypothesis in which electronic order sustains SC behaviour have been proposed, e.g. the presence of nematicity and spin density waves accompanying SC behaviour is reported by low T measurements on FeSe. In addition observations of band diagram open the question on the role of band splitting and van Hove singularity sustaining SC behaviour [6]. In relation to the last points, we report that the physical features of the materials studied in this thesis are analysed and compared with the obtained results (see Chap.4).

A **novel ionic-gating-induced protonation technique** has been exploited in this work and here discussed (see Fig. 1.2). Here, the word *gating* refers to the field-effect transistor (FET) configuration employed, where a gate voltage is applied to induce the intercalation of H^+ and/or H-rich organic ions into the material structure [9]. This technique involves the use of an electrolytic cell in which the sample and the gate (tipically consisting of a platinum wire) are immersed. A potential difference is applied between them and an intense electric field develops at the interface between the ionic liquid and the material under study. This causes the dissociation of the water molecules absorbed by the hygroscopic ionic liquid and consequently the positive H^+ ions migrate to the sample and part of them are inserted within the layers of the sample structure. Moreover, since the samples are layered TMD materials, there is a high probability that the Positively-charged, H-rich organic ions composing the electrolyte enter the interior of the structure and remain between the material layers which are connected via van der Waals bonds.

This thesis is based on resistivity measurements that have been carried out in the laboratories of *DISAT - Politecnico di Torino*. In particular, samples were observed in low T conditions. Different technologies have been exploited to reproduce these conditions: cryocooler instrument or liquid ^4He immersion allows to reach temperature values close to the absolute 0 K, with a lowest T of ≈ 2.9 K.

Several experiments [10] [11] point out to the possibility of positive results from tuning SC phase and increasing the T_C. Moreover, they show the positive effect of H insertion into materials to induce SC behaviour at higher T. Microscopically, this is based on the assumption that additional H ions can modify the material band structure, i.e. modulate the topology of the Fermi surface (FS) by the increase of electrons in the structure, consequently modulating the microscopic behaviour of the material.

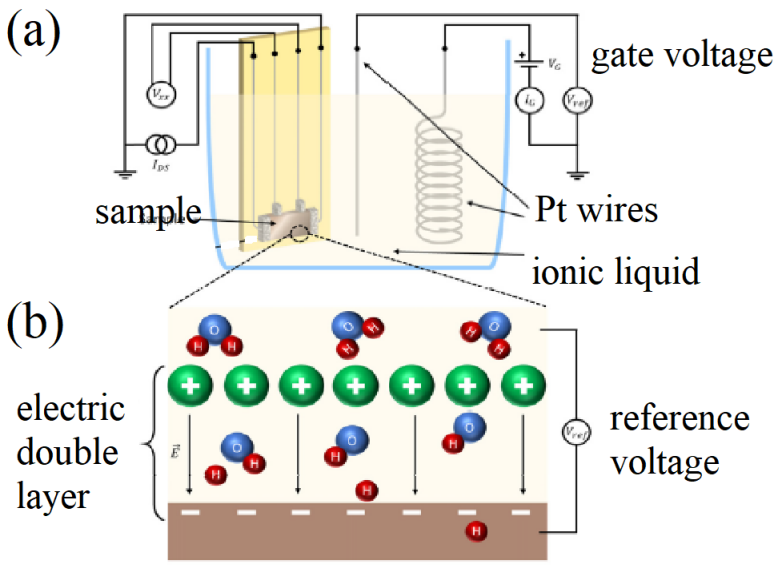

Figure 1.2: *The employed novel ionic-liquid-gating protonation technique. Gate voltage is applied to the gate contact immersed in the electrolytic cell. Consequently, the electric field is induced in the electric double layer (EDL) and it polarises the interface between the sample and the ionic liquid (solid-electrolyte interface). The electrolyte dissociation drives the H^+ ions into the sample. Low gate potential of $V_G \approx 3$ V is imposed at room or higher T. The time evolution of the process is monitored and the change on transport properties are visible thanks to resistivity measurements. Gate charge measurements allow to estimate the H^+ ions loaded in the sample. Moreover, gate voltage, gate current and reference voltage are measured during the gating process. Silver (Ag) contacts are incorporated on the sample for the measurement of 4-wire resistivity. The setup can also be mounted in the cryostat to perform quenching of the loaded H^+ ions and low-T measurements. Adapted from Ref. [9].*

Many experiments [11] have shown that protonation may affect different **microscopical properties** of the original material, such as crystal structure, electronic bands, phonon spectrum and electron-phonon coupling. The difficulty and challenges for future and current research concerns the comprehension of the phenomenon or combination of phenomena essentially responsible for SC behaviour [9]. Various protonation experiments are possible: varying T or gate voltage conditions. It is difficult to identify the optimal conditions. A tricky point is the time permanence of H in the material undergoing protonation. To avoid the H ions leaving the

structure, in-situ protonation can be performed. Here T dependent measurements are collected on the sample immersed into the ionic liquid, not to disperse H content in the external ambient. Challenges include the reduction of the complexity and the cost of the process [9].

From the perspective of theoretical models, some relevant questions are still open. How do the atomic positions of hydrogen within the pristine sample affect its vibrational properties? The effects of electron-phonon interactions concerning SC coupling, and their models could be important to guide the future experimental direction [12].

In the chapters of this thesis it will be exposed the methodology employed and the results obtained. Chapter 1 has been focused on the subject of the thesis, highlighting the choice of ionic gating technique for experimental investigation. In Chapter 2 we outline the features of TMDs, also with the aim of clarifying the reason for selecting this class of materials, in particular discussing the available literature results concerning doping and intercalation of TMDs. Chapter 3 will cover the methodology used: the measurement methods and instruments used in the laboratory. In Chapter 4 are presented the results obtained in the four materials: TaS_2, VSe_2, $NiTe_2$ and WSe_2. In Chapter 5, the conclusion reports the results and deductions from the whole of this research work.

Chapter 2

Transition metal dichalcogenides: an overview

2.1 General properties and recent research

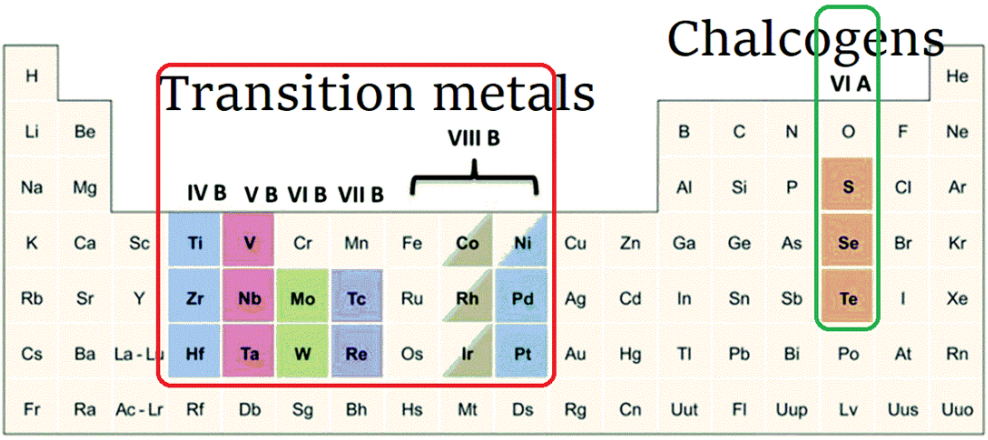

Figure 2.1: *TMDs are compounds of transition metal and chalcogen elements: these elements are put in evidence on the periodic table. Adapted from Ref. [13].*

Transition-metal dichalcogenides, TMDs, are layered materials composed of a transition metal elements mostly from groups IV, V, or VI, and a chalcogen element (sulfur (S), selenium (Se), or tellurium (Te)) (see Fig. 2.1). TMDs share a common X-M-X sandwich structure (M is a metal and X is a chalcogen). The X-M-X trilayers are connected via weak van der Waals interactions, and they can be found in a variety of structural polytypes: 1T, 1T', T_d, 2H, and 3R [7].

TMDs are a class of materials characterized by exhibiting effects of charge-density waves (CDW) formation [14]. In the context of the current research, TMDs have attracted interest because they have a relatively simple structure and they can be easily exfoliated, and they show a range of properties that can be tuned by many different methods. TMDs showed interesting features when studied at reduced dimensionality, as 2D materials, also if their hexagonal structure can not be reduced to an atomically thin layer as in the case of graphene which thickness is one carbon atom. For the properties deriving from their unique layered structure, TMDs are overtaking the popularity of pure graphene [15]. Also, the structure is similar for all TMDs but the size and the charge of both elements give significantly different material properties. Under ambient temperature and pressure conditions, the different TMDs can behave as dielectric, semiconducting or metallic materials depending on chemical composition, crystal structure, number of layers, doping level, layers' structure and strain [14]. Because of their similarities, TMDs are usually studied together and many comparative studies of TMDs can be found in literature, together with their applications. It is noted that the tendency for the formation of a 2D structure supported by van der Waals forces is most evident in the presence of heavier elements. On the contrary, TMDs composed of light metals tend to form crystal structures with 3D symmetry. [15].

Our interest in TMDs stems from the fact that they appear to be promising materials for SC research. Many evidences reported that with sufficiently strong applied pressure, or by intercalation with a variety of organic or inorganic materials, the CDWs are suppressed, and the superconductivity either appears, or it is enhanced. Moreover, TMDs compounds share many **common features with high-T_C superconductors** classes of materials, as cuprates, organic layered superconductors, cobaltates, and iron-based pnictides [14]. Relevant common features that can support the SC behaviour are: the presence of layered structures, CDW phases, pseudogaps and the possibility of a dimensional crossover from bulk to monolayered structures [16]. In the specific, the electrolytic intercalation of TMDs with water and metallic ions leads to compounds with very similar properties to cobaltates and hydrated cobaltates.

Cuprates are materials made of layers of copper oxides (CuO_2) alternating with layers of other metals oxides, which act as charge reservoir. Nowadays they are the highest temperature superconductors discovered at ambient pressure conditions [11]. The similarities of TMDs with cuprates relate to the pseudogaps present in the electronic structure. As a matter of fact, the term pseudogap refers to an energy range in the proximity of the Fermi level which has few states associated with it and it is a feature specifically observed in high-T_C superconductors. More in general, the term gap indicates an energy range that contains no allowed electron states. Pseudogaps can open up when electrons interact with the lattice. This phenomenon have been observed in a region of the phase diagram of cuprate high-T

superconductors in doped samples at T above the SC transition temperature [17]. In order to cite a relevant example, it is reported that the presence of the pseudogap in 2H-$NbSe_2$ TMD affects the CDW phase, bringing to highly anisotropic orbital symmetry [16].

Moreover, similarly to the cuprates, TMDs have the peculiarity of being layered materials where the interlayer bonds are weak and they are represented by Van der Waals forces, for this reason TMDs are also called Van der Waals materials. Additionally, the building blocks that constitute the layers can have different topologies, i.e., octahedral or trigonal prismatic, these different topologies are called **polytypes**. The TMDs structures organise in many polytypes, depending on the small differences in formation energies. The most common polytypes are the 1T, 2H(a), and 2H(b) forms, which respectively consist of identical octahedral layers and two types of trigonal prismatic double layers, as it is represented in Fig. 2.2. In general, the 1T phase tends to be less stable and to transform into the 2H phase, this phenomenon happens mainly in lightweight TMDs [18].

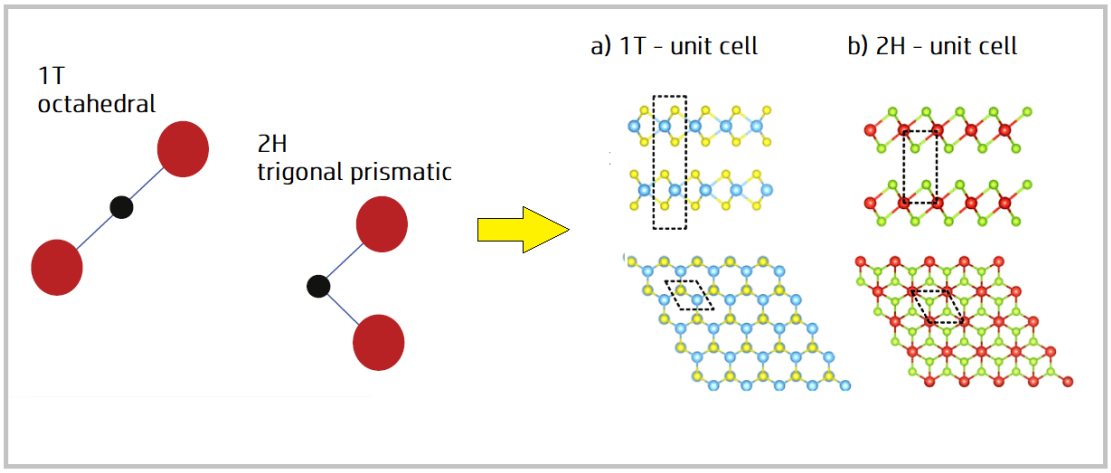

Figure 2.2: *TMD polytypes are defined according to the coordination of the atoms in each layer. In the image is visible the typical hexagonal structure of each layer, that is found also in graphene structure [15].*

The presence of CDW behaviour is a common feature of TMDs [19], and differently from TMDs, many organic high T_C superconductors, as cobaltates are free of any CDWs. As reported in the results part of this thesis, CDWs have specific characterization. In fact, they can be either commensurate (C-CDW), nearly commensurate (NC-CDW), or incommensurate (IC-CDW) with the lattice, they can rarely exhibit gap nodes and they can compete with the superconductivity in the temperatures below T_C. In summary, TMDs are a class of layered materials, they exhibit common properties with high-T_C superconductors class of materials

and their intercalates show many unconventional SC and normal state properties [14].

2.2 CDW and SC phases in TMDs

A key topic of research concerning TMDs is oriented on exploiting different methods in tuning the CDW and SC phases, inspecting microscopical electronic behaviors and their relation with the presence and interplay of these two phases. The methods can include doping [20] [21] [5], gate voltage application [22] [23], photo stimulation [24], pressure application [4] [25] [26], study on structural defects [27], study on the construction of samples [28], and thickness reduction to *nm* [29] [8]. This thesis is exploiting the effects of H insertion in the TMD structures, in order to analyse their effects on tuning their electronic properties and establish a platform to achieve ambient-pressure H-induced superconductivity.

Microscopical explanations for CDW phases describes the collective charge transport of an ordered quantum fluid of electrons in a linear chain compound or in a layered crystal. In low-dimensional structures such as layered materials, the wave-like nature of electrons can more easily cause the charge density to become spatially and periodically coupled. CDW phases are structural phase transitions, deriving from coupled electronic and ionic rearrangements. In other words, the rearrangement of the ion cores during low-temperature CDW transition produces periodic fluctuations in the electron density, called CDW and their presence has been verified in several materials [30]. Electrons in many metals can be considered as a weakly interacting quantum gas of quasiparticles. Low-dimensional metals are often unstable to the formation of energy gaps at Fermi level (see Fig 2.3), caused by a reduction of the energy of the highest filled electronic states (as compared to their original value in the non-distorted structure) when some modulationsoccurs on the electron momentum value at at Fermi level. This reconstruction happens at a specific value of T, which is then defined as the CDW transition temperature [30].

As a consequence, the CDW is a static modulation of conduction electrons and it is usually accompanied by a periodic distortion of the crystalline periodicity of the lattice (see Fig. 2.3). However, the wavevector of a CDW is determined by the Fermi surface of the material and it is not necessarily an integer fraction of a reciprocal lattice vector of the reciprocal lattice. Consequently, the incommensurate phase (IC-CDW) may result, as it is considered to have lost its translational symmetry. While the temperature decreases, the lattice may undergo a further distortion, that makes CDW to be commensurate (C-CDW), namely the CDW wavevector is an

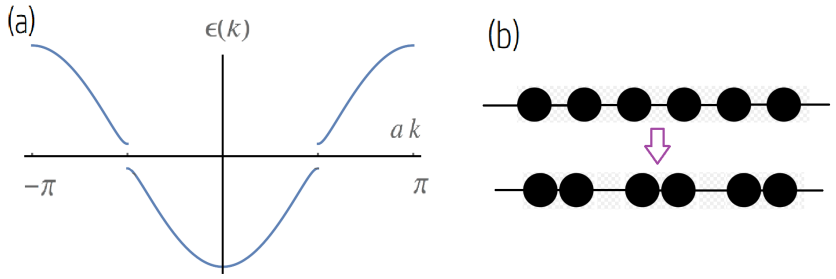

Figure 2.3: *(a) Energy gaps are presented on 1D band diagram. This feature is at the origin of CDW behavior. Considering 3D Fermi surface (FS), the contours coincide when shifted along the CDW wave vector: for this reason CDW are considered to be FS nesting-derived [31]. (b) Real lattice atoms rearrangements during the formation of CDW. Adapted from [32].*

integrer fraction of the reciprocal lattice. So, it is possible to observe different CDW transitions in the same material, as for example it is shown in the case of $1T-TaS_2$ (see Fig.2.4): at T $\approx$ 235 K there is the C-CDW to NC-CDW transition, at T $\approx$ 355 K there is the NC-CDW to IC-CDW transition, and at T $\approx$ 550 K the transition from IC-CDW to a normal metallic state occurs. Each of these transitions induce a different restructuring of the non-distorted bandstructure (see Fig. 2.5) [32].

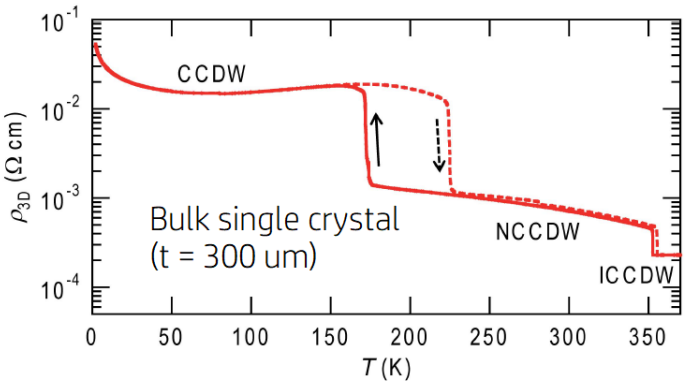

Figure 2.4: *Measurements on the resistivity of bulk $1T-TaS_2$ pristine sample. The CDW phases are visible, showing the low-temperatures transition from C-CDW to NC-CDW and the high-temperatures transition from NC-CDW to IC-CDW [8].*

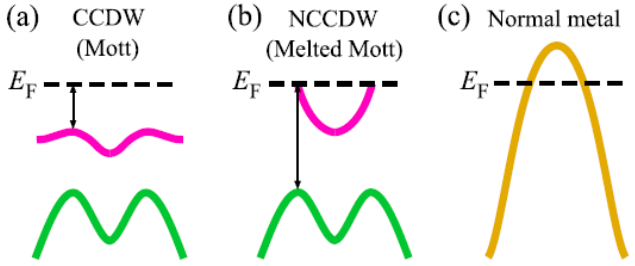

Figure 2.5: *Band diagram related to CDW phases [7]. As showed by the gap presence and the position of E_F, C-CDW corresponds to an insulating behavior, the so called Mott insulator, while other CDW phases are metallic.*

2.3 Intercalation in TMDs

Various researches concerning the intercalation in TMDs are encountered in the literature. The present research aims at further investigating the results obtained through intercalation of H and H-rich organic ions in TMD materials. In this regard, in the next paragraphs, the previous researches concerning intercalation in TMDs are described, both mentioning intercalation in general and focusing on the intercalation of H and H-rich organic ions.

With few exceptions, in most known examples of the 1T polytype the pristine TMD materials were never found to be SC at ambient pressure, and their pristine state transport properties were found to be semiconducting at room temperature or above. This non-metallic behavior is due to the formation of CDW that opens up a gap or a pseudogap over the Fermi surface for temperatures close to room temperature [34].

A large number of layered superconductors were obtained by doping (or intercalating). Different studies report that the resulting intercalation compounds were very air-sensitive and rather 3D in their properties.
The intercalation on TMDs was firstly approached by the insertion of **organic compounds**. A first work obtaining a small increase in T_C was with the immersion of crystalline $2H - TaS_2$ in liquid pyridine at T = 470 K . In this case, it is reported that the crystals grew visibly as an evidence of the effective insertion of the intercalant inside the layered structure. As it is generally involved by doping technique, many intercalations consist on charge transfer from the intercalant to the host TMD. The charge transfer was found to be facilitated by the presence of water, as in the case of the immersion of the TMD in liquid pyridine [16]. At this purpose, neutron scattering, electron diffraction, and nuclear magnetic resonance (NMR) studies of the TaS_2 indicated that the nitrogen (N) atoms contained in the pyridine molecules were placed in the middle between TMD layers, so that

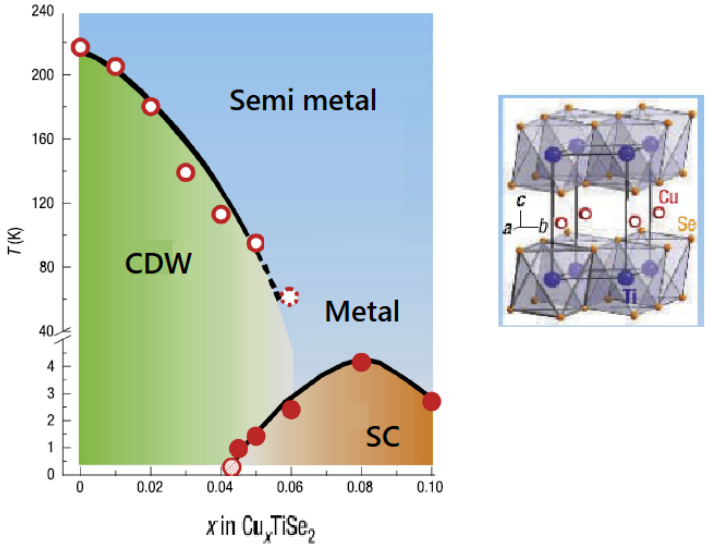

Figure 2.6: *The phase diagram of the intercalated TMD Cu_xTiSe_2 shows that the pristine $TiSe_2$ presents SC behavior under Cu intercalation, as reported by Morosan et al. (2006) [33]. Small amounts of Cu intercalation suppress the CDW and the semi-metallic state of the pristine TMD, leading to superconductivity in Cu_xTiSe_2 for $x > 0.02$, with a maximum $T_C = 4.0$ K at $x = 0.08$.*

the planes of the pyridine molecules were positioned perpendicularly to the TaS_2 layers [16]. Electron microscopy studies revealed screw dislocations in the host TMD layers and it results that screw dislocations cause the TaS_2 layers to exfoliate upon intercalation. At this purpose, it is reported that the intercalation procedure leads to a mixed-phase composition of the structure presenting different c-axis values with respect to the pristine material and the difficulty in making single-phase structure could lead to the material exfoliation under intercalation [35]. It was observed that single-phase intercalated compounds had a reduced tendency for exfoliation upon intercalation. A particular feature was observed in critical field studies: the intercalated $NbSe_2$ was observed to undergo dimensional crossover from 3D to 2D behavior in correspondence of T_C, namely, upon intercalation the material can switch from bulk to monolayer properties [36].

Regarding the intercalation on TMD, it is noticeable to cite the class of **Lewis bases**, that could intercalate into a variety of TMDs creating dative bonds. Lewis bases are molecules or ions that have a filled orbital containing an electron pair which is not involved in bonding and so it may form a dative bond. For example, NH_3 is a Lewis base, as it can donate a lone pair of electrons [37]. The increase

in T_C upon intercalation of TaS_2 with Lewis bases was found to be due to the suppression of the CDWs. On the contrary, some cases are attesting that after the intercalation of NbS_2, T_C surprisingly decreased from its pristine value. The supposed reason of this behavior could relate to the absence of CDW in this material, which instead presents SC gaps, which are possibly suppressed upon intercalation, leading to a T_C decrease, instead of an increase, as it was expected [14].

Another class of intercalated compounds was obtained using **transition metals such as Hg, In, Pb, and Cu**. A relevant example is reported by Morosan et al. [33]: small amounts of Cu in $1T - TiSe_2$ as an intercalant were able to suppress the CDW and the semi-metallic state in pristine TMD, allowing for superconductivity for $x = 0.02$, with a maximum $T_C = 4.0$ K at $x = 0.08$ (see Fig. 2.6). This enhancement of superconductivity by a transition metal (Cu) intercalation achieved similar results to the much earlier iron intercalation of $2H - TaS_2$, which raised T_C from 0.6 K to about 3 K in $Fe_{0.05}TaS_2$.

Hydrogen has also been reported to be effective as an intercalant for several layered compounds. The evolution of the normal-state transport properties and superconductivity was sistematically studied by the application of electron doping in bulk H_x-FeSe single crystals using an ionic liquid gating method with induced H^+ intercalation. Negligible effects are observed on the crystal structure. Different T_C values phases emerge at the increasing of the carrier concentration. Such discrete SC phases with an opposite trend of T_C were also observed in the deprotonation process, wherein the amount of H^+ intercalation is gradually decreased. This work showed that the discrete SC phases are intrinsic and related to the carrier concentrations, and the interlayer distance is not a primary factor for achieving high-T_C superconductivity. Moreover, the evolution of both the normal state transport properties and superconductivity are described as the change in FS topology induced by electron doping. It is considered that the amount of H^+ intercalation cannot be clearly quantified, and the protonation or deprotonation time is used to represent the carrier concentration. Additionally, NMR allowed to obtain important data regarding the position of the H^+ in the structure, finding them placed on interstitial sites close to the anions.[38].

Additional researches on protonation [10] report that carrier doping is found to be an effective method for tuning metal-insulator transitions and superconductivity under optimized protonation. In particular, H^+ is observed to be non-volatile and this feature allows post-gating transport measurements. Optimal conditions for the ionic-liquid-gating method are found in order to improve the superconducting volume ratio and the doping homogeneity. The best protonation temperature is found to be 350 K (higher than the room temperature), with a long gating period of 12 days. In these conditions the superconducting volume ratio of FeSe samples

is largely enhanced compared to the room temperature protonation results [10].

Finally, preliminary results of intercalation on other layered compounds report that superconducting transitions with $T_C \approx 15$ K for ZrNCl, ≈ 7.2 K for 1T-TaS_2, and ≈ 3.8 K for Bi_2Se_3 are induced after protonation [6].

Chapter 3

Experimental techniques

3.1 Resistivity measurements

As mentioned in the introduction (see Chapter 1), resistivity is the measured macroscopic property that gives information on the microscopic mechanism characterizing the transport of electric charge. Moreover, a sudden drop in resistivity value is registered at T_C in the material where a transition to SC phase is present. In experiments, samples typically have low dimensions (on the order of a millimeter in size), thus measuring their resistivity is a process that must be adapted to these constraints. To this purpose, a few paragraphs will be here devoted to the technique by which contacts and instruments are employed to measure the resistance of our samples.
The electrical resistance (R) of a material is defined as the ratio of the voltage (V) applied to the electric current (I) which flows through it. If the resistance is constant over a considerable range of voltage, then Ohm's law (see Eq. 3.1) can be used to predict the behavior of the material. The factor in the resistance which takes into account the nature of the material is the resistivity (ρ) (see Eq. 3.2). Although it is temperature dependent, it can be derived at a given temperature from the resistance of a sample of a given geometry. The geometry of the sample is given by A and L parameters included in the formula, they are A = cross sectional area, L = length.

$$R = V/I \tag{3.1}$$

$$\rho = R \cdot A/L \tag{3.2}$$

A nanovoltmeter is employed to measure the voltage drop between the two extremes of the sample, and the current generator is responsible for the current passing through them. The current is set to be of the order of 1 mA for conductive

samples and of 1 μA for insulating or semiconductive samples, paying attention to the fact that high current could damage the samples. The resistivity is derived from resistance measurement (Eq. 3.2). The current flows on parallel lines throughout the sample (as it is presented in the scheme on Fig. 3.1). Our sample dimensions were generally 2 mm $\times$ 0,5 mm for the surface, and 0.025 mm for the thickness, and the sample is obtained from a foil or pieces of the selected material. A constant relationship is obtained between the sourced current and the measured voltage, equally the I(V) function increases linearly and the resistance is thus reliably measured. The length of the sample is considered as the distance between voltage contacts and it is measured from the microscopy image using the microscope grid. The software *ImageJ* [39] is used to extract dimensional values from the microscope photos, and measurements are rescaled considering the microscope magnification power.

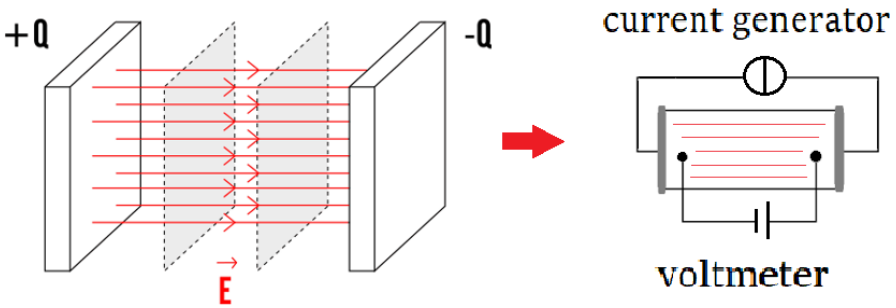

Figure 3.1: *The sample and the current flowing through it in parallel lines. To obtain a uniform flux, current contacts on the sample must cover the entire section of the sample. This creates equipotential surfaces on which voltage is measured by the voltmeter. The current is sourced by the current generator. Adapted from [40]*

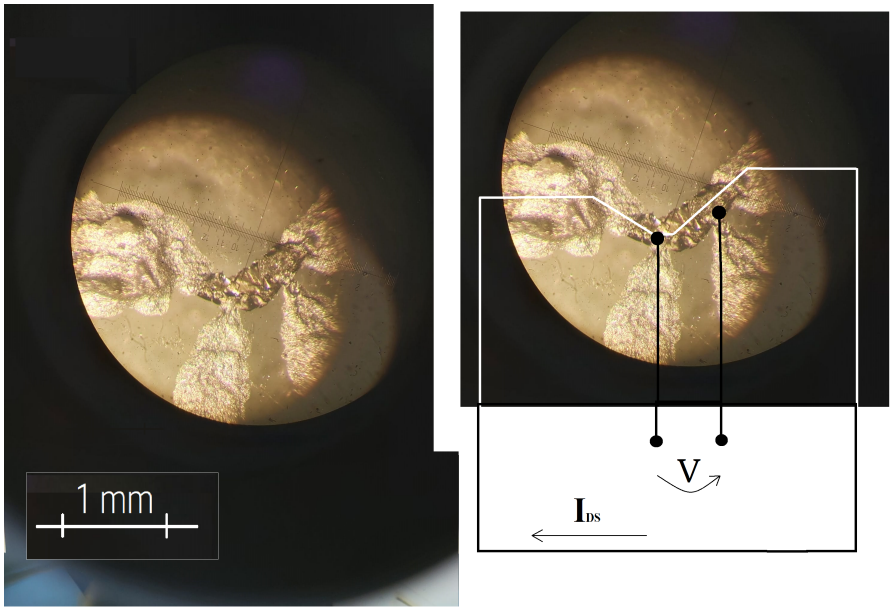

Figure 3.2: *Contacts on the sample are arranged in a four-wire configuration, e.g. here is shown the microscopy image of TaS_2 sample, where contacts are made by water-based silver paste. Black lines represent schematically the voltage wires and the voltage path along the silver contacts. Black spots represent voltage contacts placed along current path. White lines represent the current wires and the current path throughout the silver contacts and the sample.*

The problem is that the cables connecting the instrument to the sample have a higher resistances with respect to the low resistance of the sample. A four-wire configuration, or four-probe configuration, is here necessary (see Fig. 3.2). The four-wire measurement makes it possible to eliminate the systematic error due to the presence of wires and contact resistance, which in most of our cases is much greater than the sample resistance. This is because the physical separation of the circuit for feeding the current from the one for measuring the voltage drop in the sample makes negligible the voltage drop in the cables and contacts of this last circuit due to the extremely high input resistance of the nanovoltmeter. This simple mechanism is shown in Fig. 3.3, where a comparison between 2-wires and 4-wires configurations for resistance measurements is presented. In addition voltage contacts must not overlap currents contacts. In the case this happens, measurements would not be reliable, as the measured voltage would consider also the voltage drop over the silver current contacts, not only the voltage drop over the volume of the sample. Moreover, voltage contacts need to be placed as far apart as possible in order to reduce the influence of the uncertainty of the width of contacts, compared to the total distance between them.

The current inversion method is used to eliminate common-mode errors such as thermoelectric voltages and contributions from gate current.

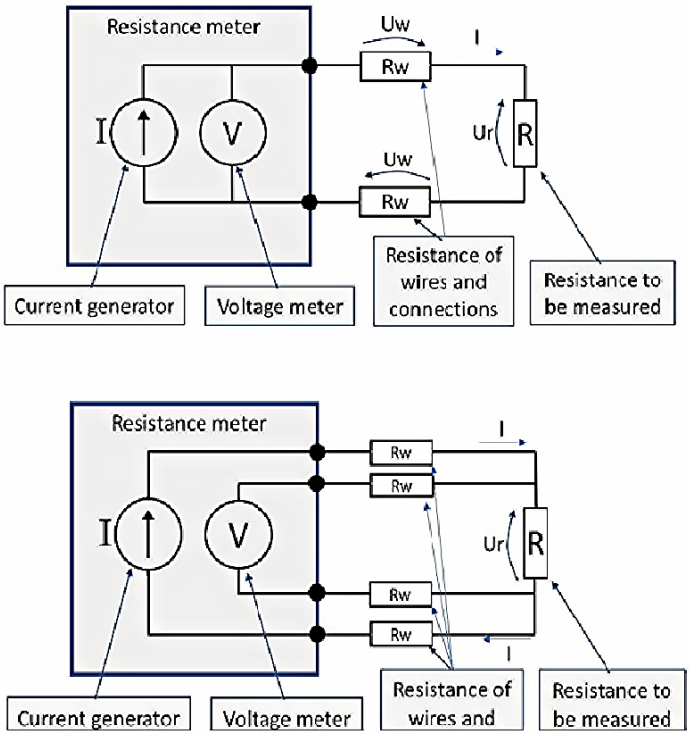

Figure 3.3: *(a) Two-wire and (b) four-wire configurations for resistivity measurements. Adapted from [41]*

The connections between the instrument and the sample are constructed using different materials. The sample is glued by an insulating glue, on a glass board (glass is a dielectric). The path that constitutes the contacts is made by different materials: in order, lines of silver water-based paste and silver epoxy paste, gold wires, indium and tin strips (see Fig. 3.4) and it terminates on isolated copper wires that can be connected to voltmeter, current generator or voltage generator (gate contact): namely the instruments that are used for the resistivity measurement and the application of ionic gating technique at room T or above room T. For cryogenic measurements, samples are mounted on electrically insulating and thermally conductive fiberglass board.

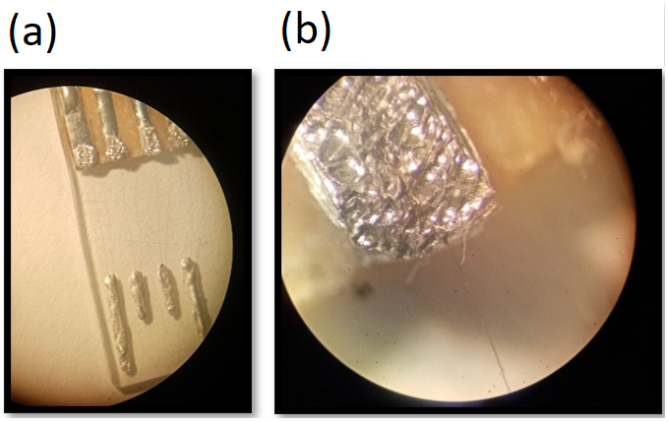

Figure 3.4: *Sample holder realization: gold wires connections(a), a gold wire fixed on the indium spot (b).*

3.2 Ionic gating

In this paragraph the two processes of resistivity measurement and gate-driven intercalation of the sample are presented.

A field-effect transistor (FET) configuration (see Fig. 3.5) [42] was realised to perform the two processes. As already discussed in previous chapters (see Chap. 1), the FET configuration consists in applying an electric field to control the flow of the current throughout the conductor or semiconductor material (see Fig. 3.6). FET is composed by three terminals: source, gate, and drain, and the application of a voltage to the gate terminal will alter the conductivity between the drain and the source. Here the gate is a coiled platinum (Pt) wire connected to the voltage generator. In our setup, drain and source contacts are at the extremes of the sample and are crossed by the current employed for resistance measurements. All components are immersed in a beaker containing the EMIM-BF_4 ionic liquid [43]. The gate is the cathode and the sample is the anode of the electrolytic cell where the intercalation occurs. A second Pt wire is also immersed in the ionic liquid cell, it is the reference electrode, whose potential difference with respect to ground monitors the voltage drop occurring at the electrolyte/sample interface. Note that not all the products of dissociation from the liquid enter the sample structure (possibly creating bonding inside the structure), but other H ions can also stay on the surface of sample or contacts, or be released in the atmosphere as molecular hydrogen gas.

Several intercalation steps are performed and the corresponding resistivity behaviors are measured. A home-made LabVIEW software [45] was employed to control all the instruments, as well as to handle data acquisition (see Fig. 3.8).

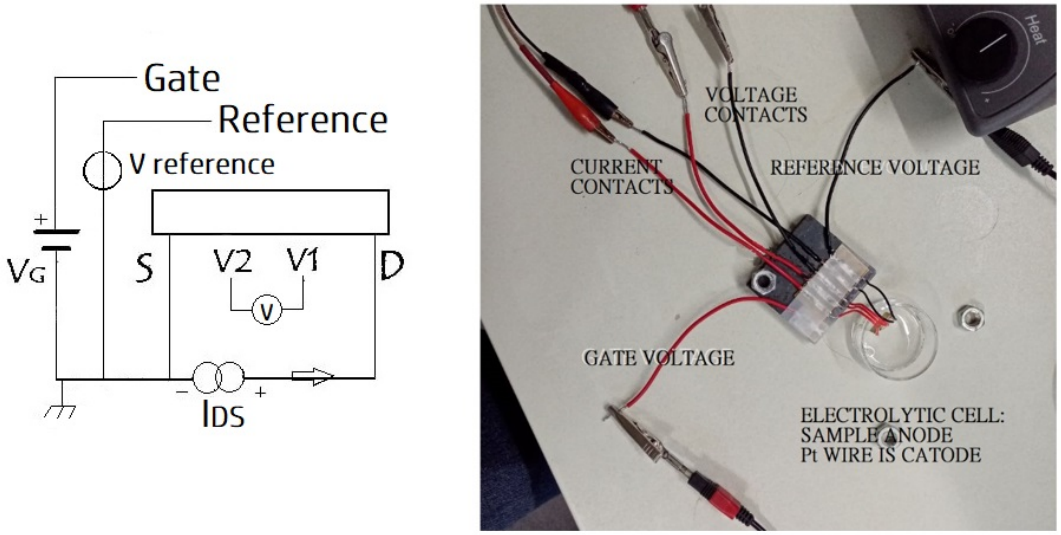

Figure 3.5: *Schematic representation of voltage and current connections in the FET configuration connected to electrolytic cell (left). Realization of the configuration (right).*

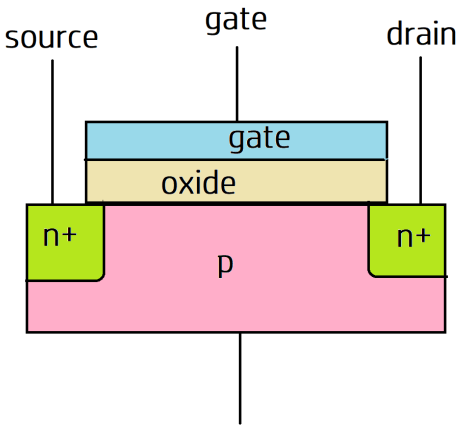

Figure 3.6: *The FET configuration involves exploiting the presence of the oxide to increase the current flowing between the source and drain contacts of a semiconductor [44]. In our ionic-gating setup, the FET configuration is realized and exploited by replacing the oxide with the ionic liquid. The metal sample replaces the semiconductor.*

Firstly, the resistivity at room T is measured in the absence of the gate and before immersion in the ionic liquid, to obtain a reference resistivity value on the pristine

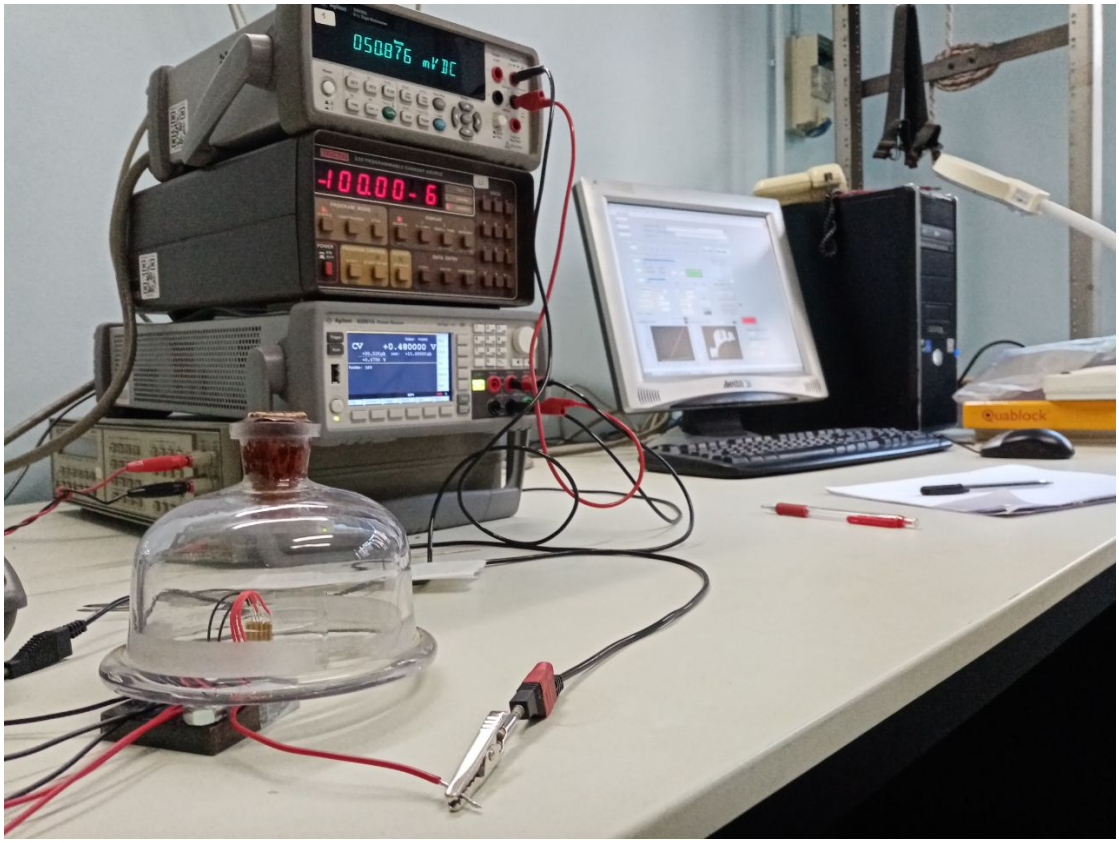

Figure 3.7: *Ionic-gating process setup. The electrolytic cell where the sample, the gate and the reference contacts are immersed. The instruments are connected to the PC and controlled via LabVIEW. The electronic instruments include the voltmeter for reference voltage measurement, the current generator for source-drain current, the gate voltage generator, the voltmeter for voltage measurement across the sample.*

sample. Next, the sample is placed in the ionic liquid and measured under open-circuit voltage (OCV) conditions, that is, without connecting the gate contact; this measurement is performed to observe the resistivity response and the effect of the ionic liquid on it. Next, the gate voltage is connected and set to 0 V; the resistivity is now measured to obtain a reference value to compare with measurements made during subsequent gate voltage applications. Next, the gate is applied in a gate sweep going from 1 V to -1 V to observe the change in resistivity and the speed of response of resistivity with respect to variations in gate voltage. Finally, a gate ramp is applied to reach the gate voltage level that induces intercalation and a stable gate voltage level is maintained (see Fig. 3.9). Under these conditions, different times are selected for performing intercalation. Commonly, 12 or 24 hours

Figure 3.8: *LabVIEW panel displaying inputs and outputs.*

of intercalation are used. It should be noted that the gate voltage level must be sufficient to activate the intercalation process, moreover a high gate voltage level is capable of inducing a larger and faster increase in the intercalation level. Too high gate voltage, however, can activate undesirable electrochemical reactions with the sample, which can induce its even complete degradation. Temperature-dependent resistivity measurements are then performed after each intercalation process.

3.3 Cryogenic T measurements

After the introduction of H or H-rich ions into the samples, the properties of the samples were checked varying the temperature. This allowed the comparison of the resistivity trend of the pristine sample with the resistivity trend of the intercalated sample, associated to different levels of H intercalation. Thus, the resistivity is measured as a function of T, varying between ambient T ($\approx$ 300 K) and T near absolute zero (T = 2.6 K - 4.2 K). The minimum temperature that is reached depends on the instrument used to cool the sample. The different cryogenic techniques will be described in the next sections.

The characteristics of the resistivity curve are observed as a function of T. It is possible to observe the presence of variations in the trend due to the insertion of the H ions, such as the presence of CDW observed in TaS_2 and VSe_2 (see

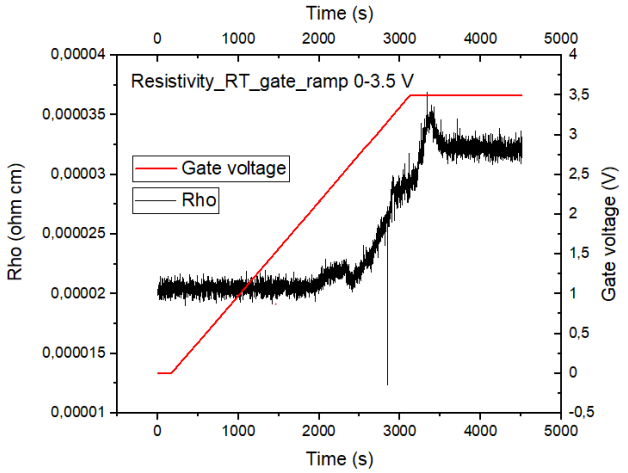

Figure 3.9: *Simultaneous time evolution of the applied gate voltage (red line) and the measured resistivity of Pd at room T. The resistivity increases during the V_G ramp and it becomes stable on flat V_g. Plots are visible on LabVIEW interface during the experiment.*

Figure 3.10: *Sample holder mounted inside the cryocooler before the closure of the cryochamber. Contacts are connected to the sample, in order to perform measurements during the cooling and heating phases.*

Chapter 4), and to verify whether there is a T_C at which the transition to the SC state takes place. During the entire process of intercalation and T dependent measurements, there are some critical moments in terms of loss of intercalant content and persistence of protonation level. In some cases, during the ionic gating process, it is observed that ions can dissolve again inside the ionic liquid when gate is switched off and the intercalants leave the sample structure. To minimize

this effect, the sample must be extracted from the ionic liquid before the gate voltage is removed. But it is possible that ions are again de-intercalated after the end of the ionic gating process. The intercalated phase may be unstable. For example, Pd has a tendency to lose the inserted H because of their diffusion in the structure, but evidences report that the stabilization of protonation can lead to reach high-T_C phase. A stabilization method can be the rapid quenching of the protonated sample to low T. To avoid the problems related to the loss of intercalant content, in-situ protonation measurements can be performed. This means that the ionic gating is performed during the heating-cooling process. It is done inside the cryocooler instruments, in order to keep the samples inside the ionic liquid with the applied gate during the variation of the temperature (see Fig. 3.11). In this way, in principle, H content is not lost when the setup is changed from ionic gating to cryomeasurements.

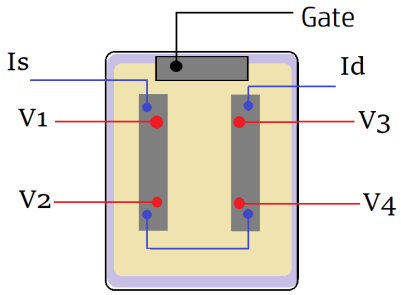

Figure 3.11: *Sample holder for in-situ protonation / cryomeasurements with gate, contacts and two samples in series. The samples are covered by the ionic liquid to perform protonation during T-dependent measurements.*

The next paragraphs outline the cryogenic techniques used. Two different instruments are used during the experiments described in the present thesis: a pulse-tube cryocooler and the ^4He dewar.

3.4 Pulse tube cryocooler

In the research laboratory of the DISAT department [47] the instruments for cryogenic field effect measurements are available and employed in this work. They include:

- a pulse-tube cryocooler for measurements down to 2.6 K (with thermometers),
- an integrated pumping systems for high vacuum (a diafragm pump and a turbomolecular pump),

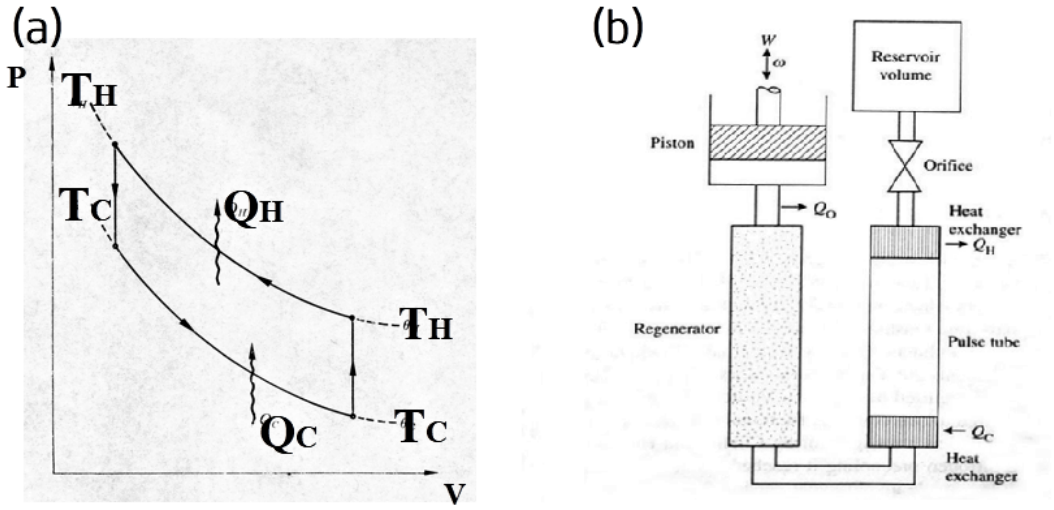

Figure 3.12: *(a) The Stirling cycle and (b) the schematic representation of pulse tube cryocooler components [46].*

- the remote-controllable complete instrumentation for electrical transport measurements and field-effect experiments as a function of temperature,
- the compressor for the pulse-tube cryocooler.

To carry out temperature-dependent measurements, the sample is placed inside the chamber of the cryocooler. Inside the chamber there are the wires that allow the sample to be connected to the electronic instrumentation to measure its resistivity. In addition, the connection to the voltage generator is present and it is used in the case of in-situ protonation, in order to apply gate voltage to the sample during temperature-dependent measurement. It is also possible to measure the resistivity on two channels and this possibility is useful for measuring two different samples at the same time or for measuring a single sample in the van der Pauw configuration that requires at least 4 voltage contacts on the sample. Two thermometers are placed inside the cryocooler chamber: one on the top of the cold finger and one on the back of the copper sample holder (see Fig. 3.10). The first monitors the T imposed by the instrument and the second provides information on the T actually reached by the sample. They normally differ by only a few tenths of a degree. To start the cooling process a 10^{-5} bar vacuum level (middle vacuum) is needed, i.e. of the order of $10^{-2} mbar$. At this purpose, a diaphragm vacuum pump and subsequently a turbomolecular vacuum pump are employed to get the necessary vacuum level by extracting air molecules from the chamber. Only in the proper vacuum condition it is possible to reach the required base (minimum) temperature. The vacuum environment prevents water and other gas molecules to ice on the

surfaces when the T decreases.

The technology of the pulse tube cryocoolers is based on periodic (pulsed) phases of pressurization and expansion of a gas at a frequency of about 1 Hz. The gas employed in this kind of refrigerator is He4 and these phases correspond to heat exchanged between the gas and the environment. In particular and roughly speaking the compression pulses correspond to a release of heat Q_H to an heat exchanger at a constant high T, while the expansion ones correspond to an intake of heat Q_C from an heat exchanger at a constant low T (that is the temperature we want to reach in the cold finger). In other two phases of the periodic process the gas passes through a regenerative heat exchanger that stores a certain amount of heat and then releases it again to the gas at the next passage. As a consequence, always roughly speaking, the thermodynamic Stirling cycle (see Fig. 3.12 (a)) models the behavior of the ^4He ideal gas during this thermodynamic process. The instrument components are schematically represented in Fig. 3.12 (b).

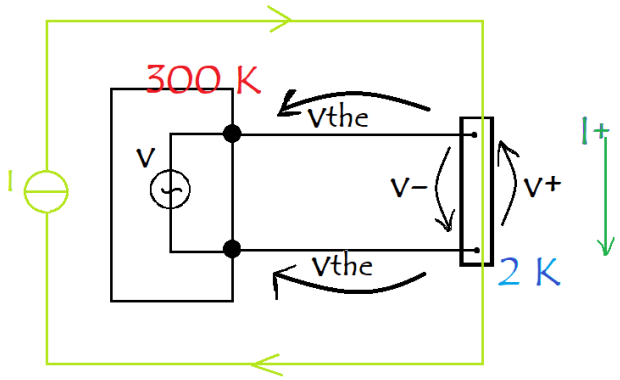

Figure 3.13: *Seebeck effect acting on cables connecting cryochamber (low T) to instruments (RT).*

When the sample is situated inside the cryocooler, the thermoelectric **Seebeck effect** needs to be considered. There is a huge T difference between the external and internal portions of the cable connecting the sample to the instruments, and it can affect measurements. The effect depends on the temperature difference, ΔT, between the two extremes of the cables, that causes an extra ΔV to the voltage drop on the sample. The quantification of the effect is expressed by Seebeck coefficient: $a_{AB} = V/\Delta T$ [48]. To remedy the presence of this error, the current reversal method is used. As described earlier in the case of measurements during the ionic gating process, here too the resistance is measured by letting the current flow first in one direction, and then in the opposite direction, and averaging the two results obtained.

3.5 ^4He dewar

During the thesis work, we also employed a ^4He dewar, where we loaded the sample (mounted on the measurement probe) by directly inserting it first into the cold vapors of helium and then into the liquid helium. The temperature was controlled by the level of insertion of the measurement head in the gas vapors. In general, liquid helium refrigeration methods, based on He vapor temperature, are exploited in cryostat instruments. The simple ^4He technology was here used and it allows minimum temperatures of about 4.2 K. We note that ^3He technology allows even lower minimum T to be reached, T = 0.3 K, but ^3He is a rarer and more expensive helium isotope, and its cost is much higher than ^4He. These are cryostats in which low temperatures are achieved by evaporation of the liquid helium (both ^4He and ^3He).
The cryostat consists of a special metal dewar containing ^4He, in which the chamber is immersed. The construction of cryogenic equipment needs to consider that the dewar is subject to high thermal stress. One characteristic is the high internal pressures that require the presence of safety valves. In addition, the structure requires thermal insulation in order to minimize the heat exchanged with the external environment. For this purpose, insulation is achieved by a vacuum ambient surrounding the internal chamber. Metal dewar cryostats are made of either stainless steel or aluminum, with many layers of superinsulation. In addition, there is a Cu or Al radiative shield. The structure is pre-cooled with liquid nitrogen (N_2). The cryogenic insert can be moved up and down in the vapors present above the liquid helium bath. In this way the T can vary from 4.2 K to over 250 K. The latent heat of evaporation and vapor pressure are essential properties in determining whether a liquid is useful for cooling.

Chapter 4

Experimental results and discussion

4.1 TaS_2: CDW and SC phases competition

4.1.1 Our results

Short-time gating processes. On a 100 μm thick samples, we performed a sequence of different gating processes at room temperature and then, the resistivity is measured in temperature dependence. Gating was performed on the same sample at 3 V at room temperature in subsequent intervals of 15 minutes, 30 minutes, 1 hour, 2 hours, 3 hours, 4 hours, 5 hours, and 7 hours. The measurements are showed in the graph of Fig. 4.1. The two curves with the same color refer to the same intercalation period during cooling and heating process measurements.

From the different series of measurements (see Fig. 4.1), it is observed that the pristine sample has a metallic behaviour with low resistivity at high temperature and it presents the development of the CDW phases at low T. There is a transition from NC-CDW (nearly commensurate) to C-CDW (commensurate) CDW and the transition temperature is 150 K from cooling process and 230 K from heating process. As a consequence of the different results obtained during cooling and heating processes, a hysteresis cycle appeared on resistivity measurements. After the gating process of the sample, the CDW phase in the resistivity measurement is still present and it is little affected. The main result is observed at low T in the strong increase in the resistivity at low temperatures, indicating a progressive strengthening of the insulating behaviour. This feature is observed from the measurements of gated samples for $>$ 1 hour gating time.

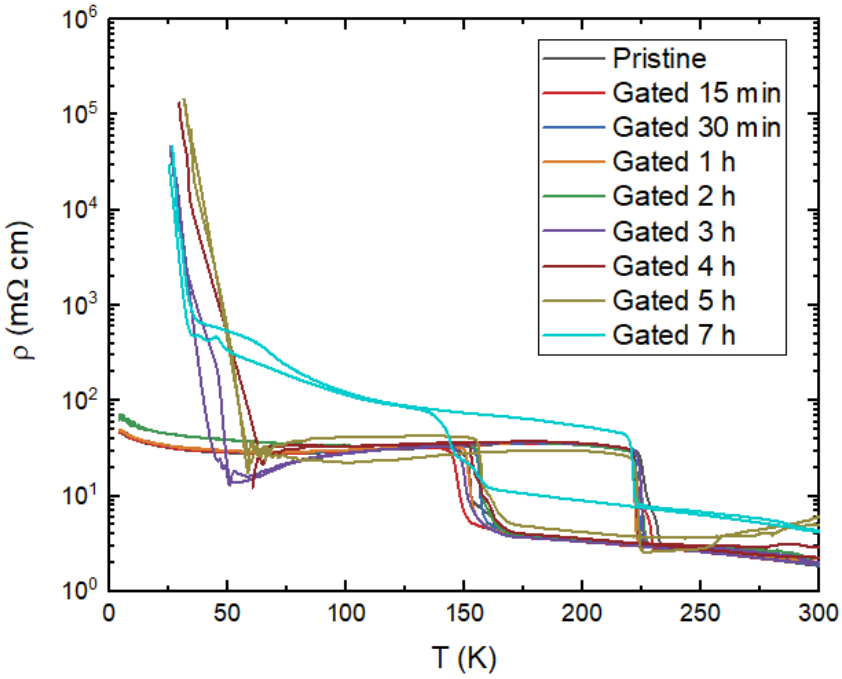

Figure 4.1: *Short time gating processes. T-dependent resistivity of* TaS_2

Long-time gating process. After the observation of the increasing in resistivity level after the 7 hours gating (see light blue curve in Fig. 4.1), we performed longer-time gating process of 12 and 36 hours. A 50 μm thick sample of TaS_2 was subjected to several gating processes at room temperature. Firstly, temperature-dependent resistivity was measured on the pristine sample using the van der Pauw configuration in the cryocooler instrument. Subsequently, ion gating was applied at room temperature at 3 V for a period of 12 hours and then for a period of 36 hours. After each gating process, temperature-dependent measurements were performed (see Fig. 4.2).

The most relevant consequence of intercalation can be seen from the long gating processes results (see Fig. 4.2). Here the pristine case shows the presence of CDW phases, while intercalation has the effect of suppressing CDWs and increasing the resistivity level. It is possible to say that the sample acquired a more insulating behaviour as doping level increases (from 12 to 36 hours intercalation) and CDWs are suppressed in the 36 hours gated sample. At low T the resistivity of the gated sample is about 6 orders of magnitude higher in comparison with the pristine sample. We have to remember that CDW are charge density fluctuations in the conduction band, for this reason the CDW are suppressed in the transition to the insulating phase, as the charge carrier density decrease to a null value.

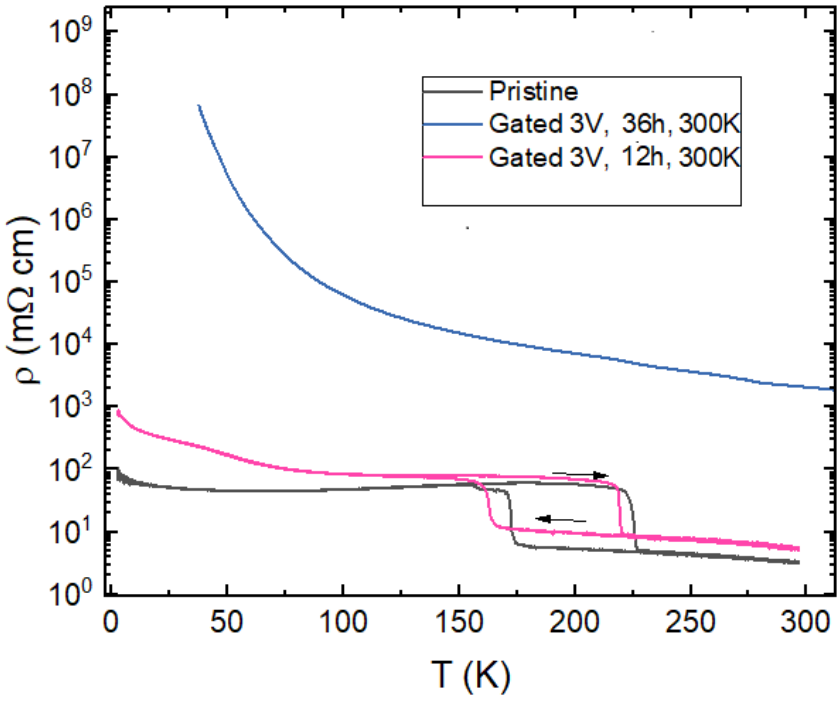

Figure 4.2: *Temperature dependence of TaS_2 resistivity measured in the cryocooler. The curves refer to different levels of protonation.*

During the experiments, the doped sample shows high resistivity at low T, CDWs are observed in pristine and doped samples. At higher gating time of 36 hours the CDW behaviour was suppressed, the resistivity increased at all temperatures and the insulating state was enhanced at low temperature. The low-temperature measurements obtained in the different set of measurements (short and long gating times at room temperature) present similar resulting features, in the increasing of resistivity level, with the suppression of CDW only in the 36 hours doped sample. We observed that the intercalation at room T did not have the desired effect of increasing the charge carrier density and the conductivity of the sample. On the contrary, when the intercalation is performed at room T, H-rich molecules only introduced defects in the structure, and they don't increase the conductivity. Consequently, there is a decrease in the mobility μ, which implies a decrease in the conductivity σ.

Gating at high temperature. Further experiments have yielded interesting results. Gating process was performed at high temperature of T = 350 K, imposing a gate voltage of 3V for 36 hours. After gating, the sample was measured as a function of temperature. From this measurement, it showed a decrease in resistivity

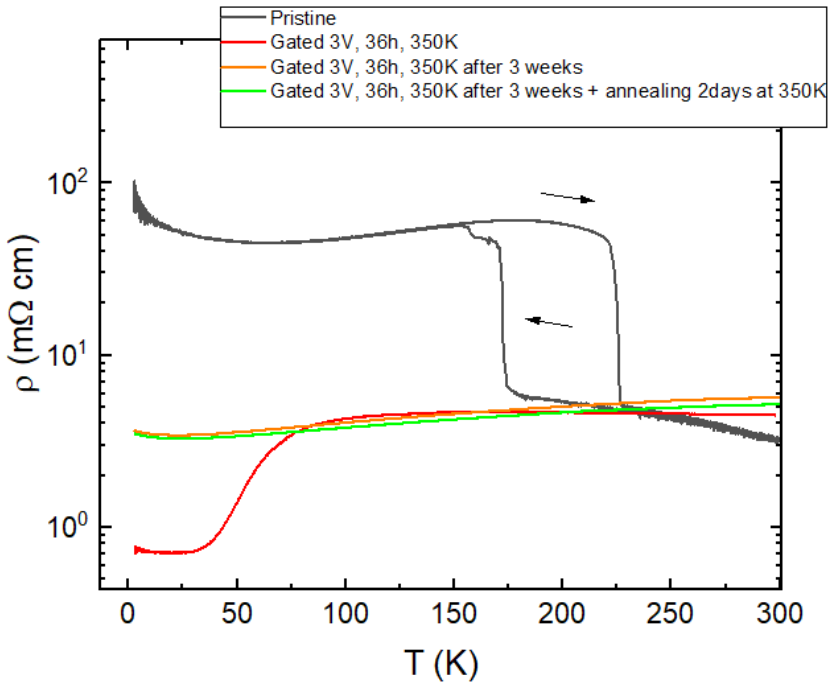

Figure 4.3: *T-dependent TaS_2 resistivity measurements. Red, green and orange curves results from samples gated at 350 K.*

that refers to the transition to a metallic state. Moreover, it was showed the suppression of the commensurate CDW behaviour (see green curve in Fig. 4.4). Interestingly, after the gating process performed at 350 K, the main observed successful features are the transition to a metallic state and the removal of the CDW. The resistivity decreased of 2 orders of magnitude at low T. So, we can deduce that the 350 K gating was able to induce a transition to a metallic phase. It is possible to say that in these conditions, the intercalation was successful in providing additional free carriers to the system as it was enhanced the metallic behaviour. Also, the volume of the sample increased after intercalation showing that H-rich molecules have been inserted in the structure.
Moreover, the stabilization of the intercalation was tested, as a matter of fact, the resistivity of the 350 K gated sample was measured again after three weeks. The results persisted in the structure after three weeks as the curve showed a similar behaviour and CDW were still not present. It is possible to deduce that the majority of intercalated H-rich molecules remained in the sample structure and they were not volatile after three weeks from the removal of gating. Only a reduced loss of intercalant content is revealed by the effects on the lowest T region, where the resistivity showed an increase.

Finally, the annealing at 350 K was successful in showing the stability of this structure when subjected to high T. As a matter of fact, the green curve (measurements after the annealing) has the same behaviour of the orange curve (measurements before the annealing) (see Fig. 4.4).
In summary, from our experiments on 1T-TaS_2, we can conclude that the most successful result derived from the high T gating process. It was able to increase the conductivity of the sample and additionally the H content in the structure revealed not to be volatile. The structure was stable for long time and when exposed to annealing at high T. For this reason, future experiments can involve high T performed gating processes, imposing longer gating periods, and imposing higher gate voltage. The purpose is to find the best combination of the parameters affecting gating process: including gating voltage, time and temperature.
Important experiments on 1T-TaS_2 protonation are reported in literature by Cui et al. [10]. They achieved successful results, increasing the T_C from 0 K to 7.2 K. It is reported that a gate voltage of 3 V is applied in the ionic liquid EMIM-BF_4 for a gating period is 12 days. The optimal gating temperature was 350 K, which improves proton diffusion in the structure. Moreover, measurements were successfully performed after gating was removed at the room T and they indicate non-volatile intercalation.
In comparison with the cited research paper [10], we can confirm the successful improvement obtained by the gating process performed at high T = 350 K, that allowed us to obtain the transition to a metallic phase. Moreover, we implement similar ionic gating conditions, including the EMIM-BF_4 ionic liquid and 3 V gate voltage level. In our case, we didn't observe the SC transition, but on the lines of the obtained results and confirmed similarities with previous researches, we consider TaS_2 is a good candidate for future research on SC. The development of our present results can include longer intercalation periods.

4.1.2 Literature results

1T-TaS_2 polytype. The TaS_2 can exhibit different polytypes structures: 1T, 2H and 3R [49]. Our work was conducted on 1T polytype.

The TaS_2 sample are bulk crystals produced from *2D semiconductors USA*, a world leading manufacturer [50]. The manufacturer guarantees about samples parameters [50]: the crystal length is approximately 6 - 8 mm, the material shows CDW phases, the crystal structure has hexagonal symmetry , the sample is produced by flux zone method used for synthesizing vdW crystals and its purity is confirmed to be over 99.9995 %. Crystals can be grown by either flux zone method or chemical vapor transport (CVT) method, but CVT method has the drawback of introducing contaminants and defects in the crystal that can influence CDW behavior on the T transition and sheet resistance. Flux zone distinguishes itself

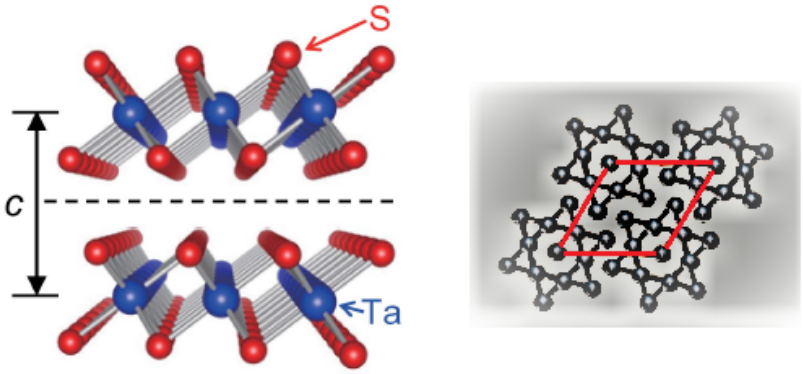

Figure 4.4: *The structure of 1T-TaS_2 polytype. The distance between subsequent Ta layers along* c *axis represents the conventional thickness parameter [8].*

from CVT technique, as CVT provides quick (around two weeks) growth but poor crystalline quality, while flux method takes around three months, ensures slow crystallization for better atomic structuring, and more impurity free crystal growth [50]. 1T and 2H polytypes of TaS_2 samples are highly crystalline vdW layered TMD, they can be exfoliated and they guarantee to show CDW behavior. Also, it is reported that 2H polytypes shows SC behaviour around 0.2 K and it exhibits IC-CDW phase below $\approx$ 80K. TaS_2 samples remains in stable conditions also if exposed to air under ambient conditions [50].

From manufacturers information it is reported that both 1T and 2H phase TaS_2 crystals exhibit CDW behavior with different T transitions: in the case of 1T it is $\approx$ 175 K and in the case of 2H it is $\approx$ 80K. 1T-phase TaS_2 exhibits three distinct CDW phases, at T above 180 K it has the so called Mott phase transition, below 354 K nearly commensurate charge density wave (CDW), between 350 K and 550 K incommensurate CDW, and metallic or semimetallic behavior above 550 K. The resistivity curve provided from manufacturers is shown in Fig. 4.5 where CDW phases can be observed. The pristine 1T polytype is insulator at ambient T and it presents CDW phases in dependence on temperature, and Mott state [27]. 1T-TaS_2 polytype structure is composed of planes of hexagonally positioned Ta atoms, alternating with two S chalcogen layers coordinating the central Ta atom in an octahedral arrangement [51].
In a general overview on TaS_2, a phase diagram reported in the literature [5] describes TaS_2 resistivity as a function of Fe doping level (see Fig. 4.6), where it is possible to observe the appearance of a SC phase within the metallic phase region of the diagram. It is possible to notice that the SC phase is restricted only to an optimal doping level. Moreover, many different methods were able to induce a SC phase in TaS_2, these methods include: pressure [4], Se doping [51], Li doping [22]

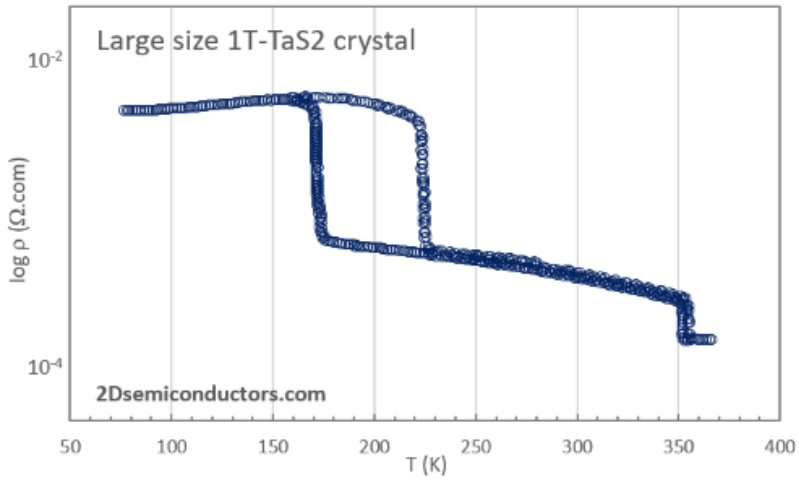

Figure 4.5: *1T-TaS_2 resistivity provided from manufacturers datasheet [50]: the sample shows CDW phases around 175 K and the distinct behaviours are visible in the figure: at $T < 180$ K Mott phase, NC-CDW at $T < 354$ K, I-CDW $T > 350$K.*

and thickness reduction [8].

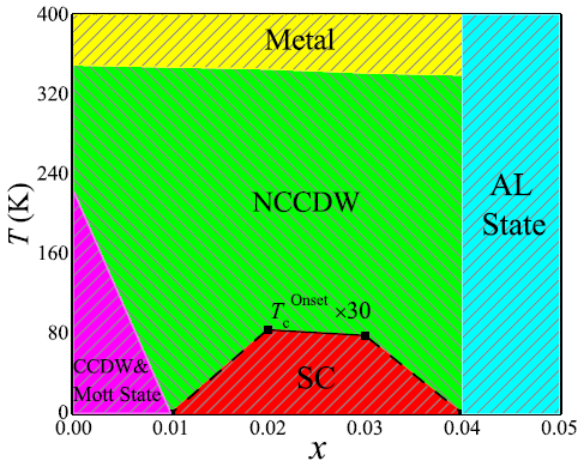

Figure 4.6: *The electronic phase diagram of 1T-$Fe_xTa_{1x}S_2$ single crystals [5].*

Extreme charge carriers concentration limit. Relevant studies are reporting on the relation between gate application and sample thickness [22]. It is reported that gate controlled in-situ intercalation of Li ions has been performed by iFET configuration on quasi 2D 1T-TaS_2 samples. The purpose was to increase the charge carriers concentration to study their extreme concentration limit in

the low dimensional structures. Results concern the observations on the role of sample thickness, reduced by mechanical exfoliation down to 2 *nm*. A critical thickness is found below which CDW order can not be sustained and both CDW phase transitions are not present (at low and high T). It is also noticeable the reversibility of the gate intercalation processes on the sample behaviour and on the charge carriers concentration. The results on resistivity measurements as a function of gate voltage and sample thickness are presented in Fig. 4.7. Moreover, it is noted that the dielectric environment and the surface impurities have stronger influences on thinner samples, according to the increased surface area over volume ratio. 1T-TaS_2 crystals have been firstly studied for their potential applications in batteries. In fact, Li ion intercalation by V_g induces structural modification, similarly to the charging process in a Li ion battery.

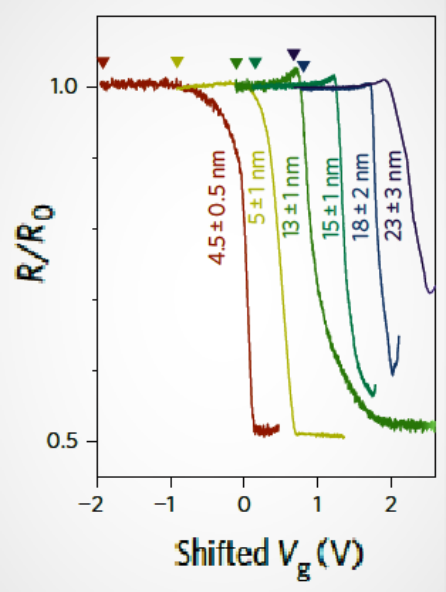

Figure 4.7: *Normalized resistivity (R/R_0), where R_0 is the RT value. R drops of half its value at $V_g = 2V$ during the high temperature CDW phase transition. Resistance R is shown as a function of V_g for few typical samples of increasing thicknesses from left to right. The gate-induced NC-CDW/IC-CDW high T phase transition is manifested as the sudden drop in resistance by one-half. Curves are shifted horizontally for clarity, and the origins on V_g axis related to each curve are marked by colour-matched triangles [22].*

SC tuning on quasi-2D nanometrical structures. Fig. 4.8 is showing the three obtained results on resistance and resistivity graphs: effects of gate voltage, cooling rate and thickness variations on samples. A super-cooled state is achieved, in which the CDW phase is suppressed. This occurs for (a) low thickness samples

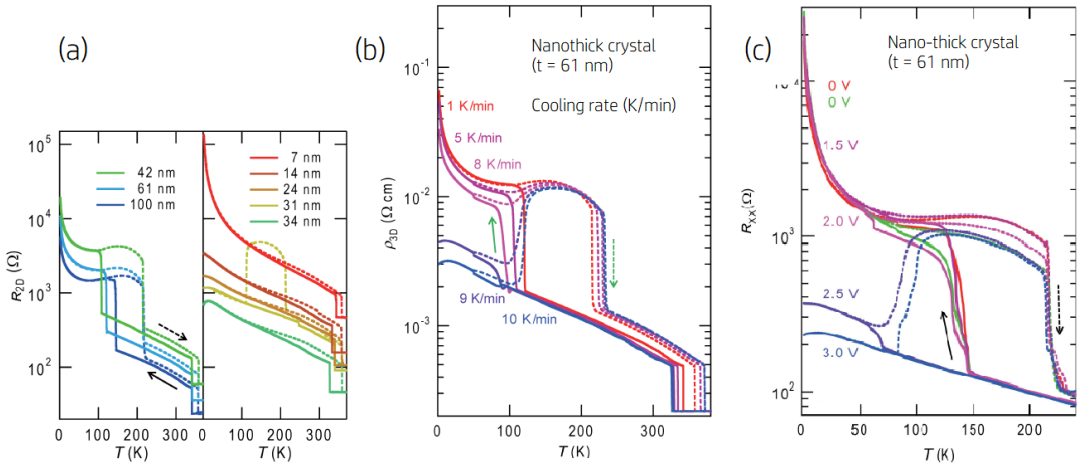

Figure 4.8: *Measurements of resistance and resistivity of TaS_2 samples. CDW behaviour is varying according to different parameters variations: (a) thickness, (b) cooling rate and (c) gate voltage [8]*

(< 34 nm), or (b) combining the effects of rapid cooling rate (< 9 K/min) on 61 nm thickness sample, or (c) high gate voltage (< 3 V) on 61 nm thickness sample [8].

High pressures. Experiments concerning the application of high pressure have yielded interesting results in the analysis of microscopic dynamics at the origin of SC [25].

The (T,p) diagram is presented, where the applied pressure reaches 100 GPa (Fig. 4.9). SC phases, can also increase the magneto-resistance at high T. Two main results are observed during the compression: firstly the change from layered to non-layered structure and secondly the microscopic change from electron-electron to electron-phonon interactions.

As the pressure increases, the 1T structure switches to a distorted 1T' structure, then it switches to a metastable non-layered structure, and finally to the non-layered tetragonal structure (see Fig. 4.9). The maximum SC transition temperature is observed only in the non-layered tetragonal structure. The relationship between CDW and SC phases under pressure is also observed by XRD and DFT calculations, allow to get more information regarding the microscopical structure. It is remarkable that the SC transition mediated by electron pairing is caused by electron-phonon interaction. The unexpected coexistence of commensurate CWD and SC phase (see Fig. 4.10) suggests that the electron-phonon coupling for the formation of Cooper pairs is the mechanism driving this behavior (obtained under pressure) [4].

Moreover, pressure dependent systems are inspected by XRD measurements [4] for the characterization of CDW behaviour composed by wave vector, amplitude,

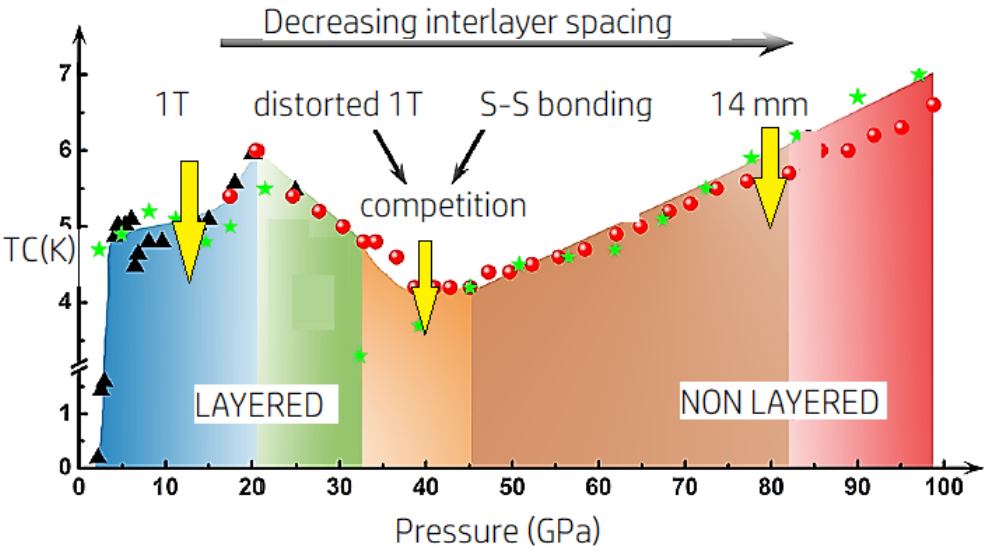

Figure 4.9: *The variations in the structure of 1T-TaS_2 under pressure [4], with relative change in T_C. The maximum T_C values relate to the non-layered structure. It is noted that the structure changes from layered to non-layered when compressed, since vdW forces are replaced by covalent S-S bonds, and the inverse transformation is observed in decompression. Red, black and green spots represents T_C measured at different pressure conditions.*

coherence length. Interesting evidences are showing that insulating C-CDW and SC behaviours can coexist in the structure, XRD measurements reports the region where C-CDW and SC are coexisting in (T,p) diagram [4]. This feature is possible because different electrons in the materials are responsible for the two different behaviours. Namely, SC and CDW can coexist in real space but they occupy different regions in reciprocal space. Therefore the research is oriented on the comprehension of circumstances that allow electronic order to competes, coexists, or supports SC.

Se and Fe doping. Fe and Se doping methods have shown to reduce the Mott gap in the transition from CDW to SC. The behavior was observed on the DOS diagram [5]. Furthermore, DFT calculation results report the evolution of T_C as a function of Fe ratio (x), from which it is inferred that there is an optimal doping level beyond which the Anderson Localization effect causes the increase of resistivity and the suppression of SC. DOS diagram shows the pristine sample (x = 0) results where CDW transitions are both visible. On the contrary for high doping level of $0.01 < x < 0.04$ SC appears and the highest obtained $T_C = 2.8$ K for x = 0.02. Also the NC-CDW phase is suppressed by introducing Fe doping.

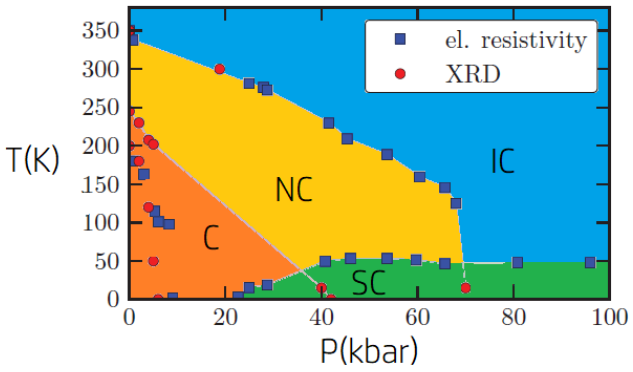

Figure 4.10: *Coexistence of CDW and SC phases in (T, p) diagram [4]. It results from different sample measurements: resistivity and XRD.*

This result is visible in ρ diagram around T = 350 K.
Selenium (Se) doped single crystals have been realized using the CVT technique with doping level of ratio $0 < x < 2$. Results are important to derive information on the interplay between electron correlation in CDW and SC. On (T, x) graph the coexistence of SC and CDW phases is never found as it is visible in Fig. 4.11,(a) [27].

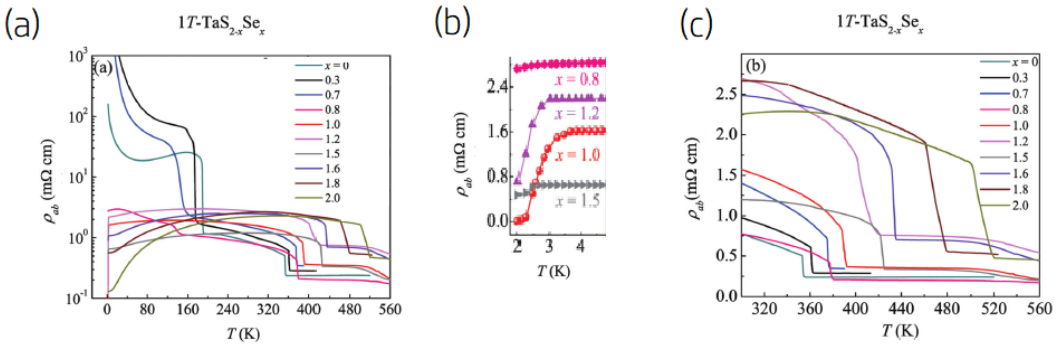

Figure 4.11: *(a) SC transition at low T in the $C - CDW$ region, for high x level of Se doping. (b) Resistivity drop in SC transition at T_C. (c) $NC - CDW$ transition at high T related to different Se doping levels [27].*

Defects presence. Finally, some researches are oriented on how the realization of samples affects their properties: generally knowledge is that $1T - TaS_2$ could be realized with quasi-2D character [27].
CVT method can be employed to realize samples and defects can be introduced by

quenching. The growth condition also influences the transition between metallic-insulator phases. It is noted that defects can destroy the long-range phase coherence and they can inhibit the metal–insulator transition. Also, they can induce lattice distortion consequently enhancing the electron–phonon interaction. Most importantly, defects are reported to suppress CDW and to induce SC with reported $T_C > 2.1$ K. Sulphur vacancies are shown to give lattice shrinkage. Different research groups are in accordance on the fact that defects can be able to induce SC by reducing Mott gap and high T_C are obtained around $T_C = 2.5$ K, while NC-CDW transition shift from 315 K to 350 K.

4.2 VSe_2: metallic behaviour and low temperature CDW

4.2.1 Our results

During the first experiment, we measured the resistivity of the pristine sample and then we performed the gating process on different samples at room temperature and after each gating process we measured the T-dependent resistivity. On the first sample we applied a gate voltage of 3 V for 48 hours. A second sample was gated at 3 V for 48 hours at 300 K and successively it was annealed at 350 K for 48 hours to test the stability of the intercalation.

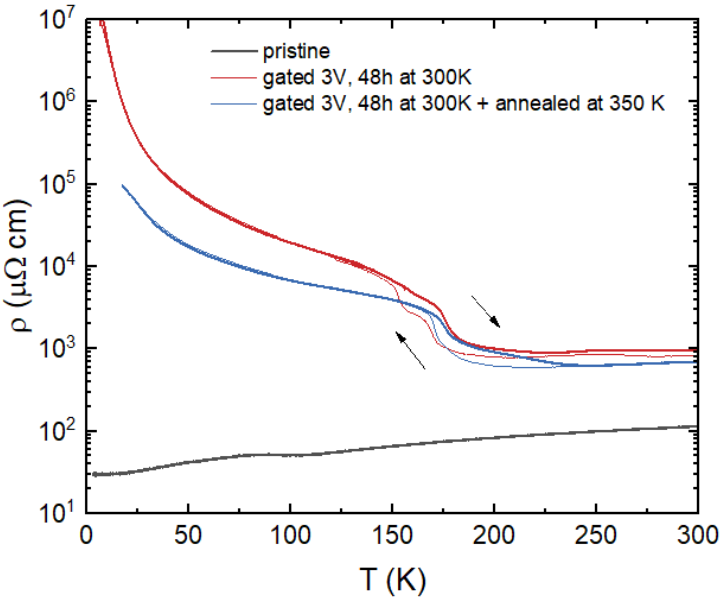

Figure 4.12: *Temperature dependent resistivity measurements of VSe_2, pristine and gated samples.*

Thickness increasing. In this samples we observed an increasing in the thickness during all the experiments, as a consequence of the increasing of gating time. In the first sample the thickness increased from 70 μm to 80 μm. In the second sample the thickness visibly increased after protonation from 50 μm to 70 μm. The reason of the increasing in thickness is attributed to the fact that the ionic-gating process induced H-rich charged molecules to migrate from the ionic liquid into the sample structure. As a matter of facts, not only H^+ ions are introduced into the structure, but also larger H-rich ions are positioned into the layers of the TMD structure. In general, the layered structure of TMDs allows

large ions to intercalate between the layers, and, for this reason, the thickness of our samples visibly increased after the intercalation process.

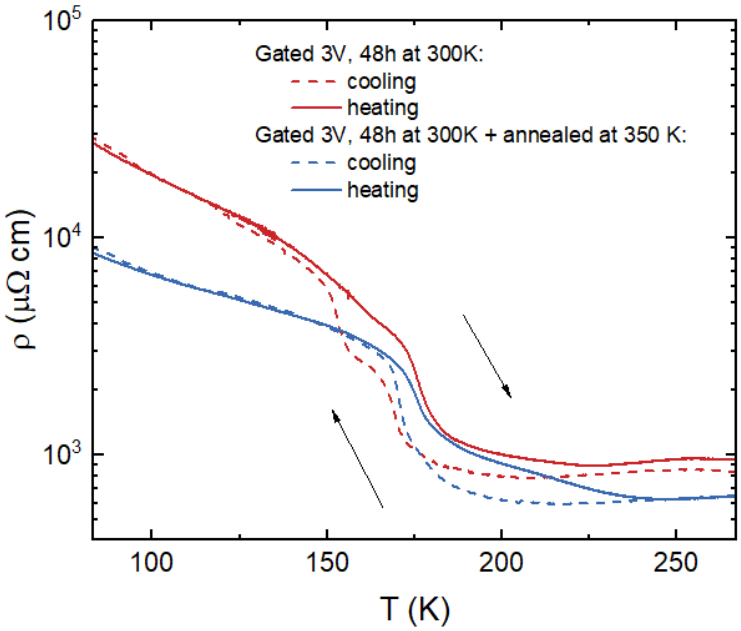

Figure 4.13: *CDW transition of intercalated samples. The first sample was gated at 3 V for 48 hours at 300 K, the second sample was gated at 3 V for 48 hours at 300 K and then it was annealed at 350 K for 48 hours.*

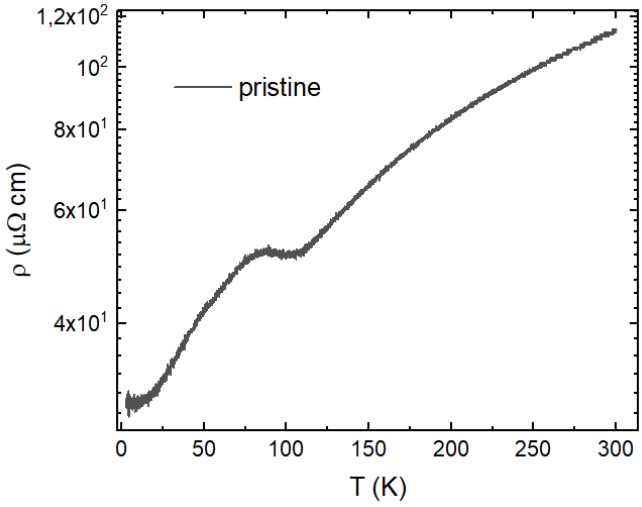

Figure 4.14: *CDW transition observed in the pristine sample.*

T-dependent measurements results are quite different in the pristine sample and in the doped ones (see Fig. 4.12). The main observations regard the increasing of resistivity from the pristine to the doped sample, the sample is assuming a more insulating behaviour after its H-rich ions intercalation. Moreover, the CDW behaviour is enhanced after gating. The resistivity of the 3 V doped samples increased of one order of magnitudes at high temperature and more then four orders of magnitude at low temperature. The second sample is gated and successively annealed. On this sample we observed a small decrease in resistivity with respect to the gated and not-annealed sample; this is related to the small loss of intercalant content in the structure during the annealing process. As a matter of facts, the annealing process was performed just to check the stability of the intercalation after the removal of gate voltage and the exposition to high T. In this case, the resistivity measurements performed after the annealing revealed that the doped structure was not totally stable, as it losses a small amount of intercalated H^+-rich ions.
In Fig. 4.14 it is possible to see that the pristine VSe_2 has a metallic behaviour, and it presents a CDW anomaly at low T, with a CDW transition temperature observed around 93.3 K.

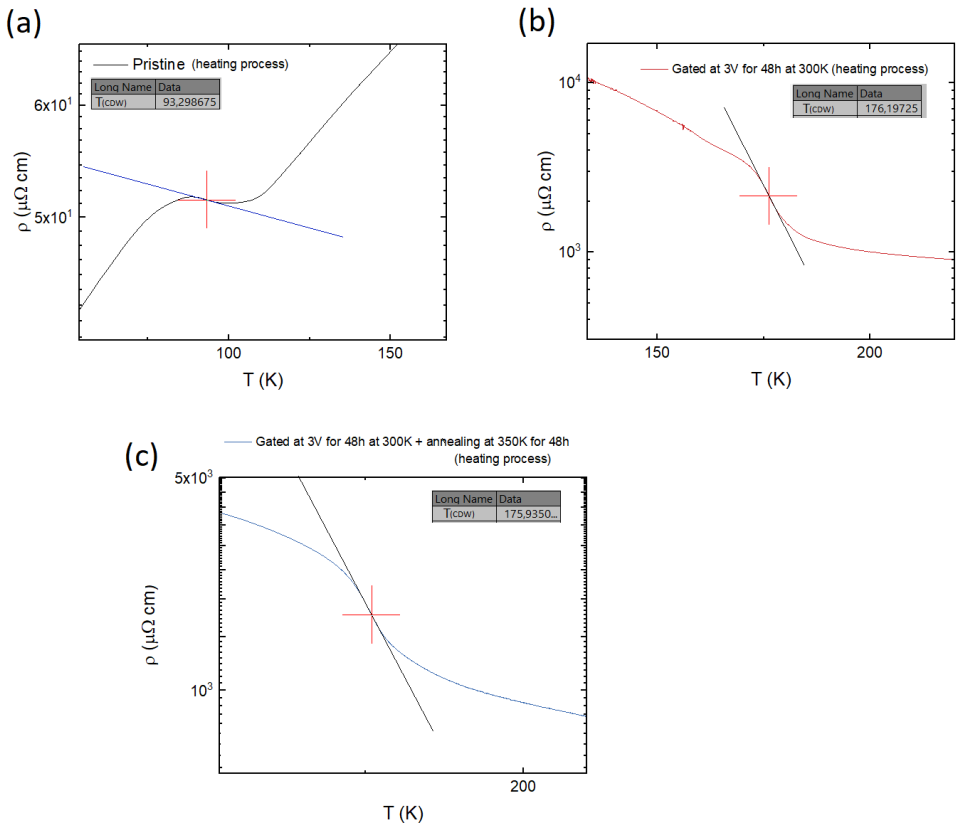

Figure 4.15: *The three plots show the CDW transition temperature of the pristine sample (a), the gated sample (b) and the gated and annealed sample (c). We performed the analysis on each curve to find the CDW transition temperature. The inflection point, is the point on the curve where the curve crosses its tangent and the second derivative vanishes. It corresponds to the CDW transition temperature.*

In Fig. 4.15 it is presented the analysis of the three curves of resistivity: the inflection point is found in order to determine the CDW transition temperature of the sample. After ions intercalation the CDW transition temperature increased: from $T_{CDW} = 93.3$ K (pristine case) to $T_{CDW} = 176.2$ K (3 V, 48 hours, room temperature gating) and then it decreased again after the annealing to $T_{CDW} = 175.9$ K (3 V, 48 hours, room temperature gating and successive annealing).
From resistivity measurements during cooling and heating processes in the same sample, a hysteresis cycle is observed. It derives from the fact that the resistivity has two different CDW transition temperatures, during the process of heating and cooling. The increasing in resistivity under gating corresponds to a transition from a metallic to an insulating behaviour.

From the interpretation of the observed features in resistivity measurements, that involved an increasing of resistivity level after gating, we must remember that the effect of doping in the material depends on the doping-dependence on the band-structure. Pristine 1T-VSe_2 is a nearly-compensated semimetal with electron-type majority carriers, but Li-intercalation induced electron doping has been shown to lead to a topological transition in the Fermi surface into an insulating state with hole-type majority carriers [23]. In this context, the electron doping introduced by the H-rich organic ions appears to induce an analogous transition in H-doped VSe_2.

In summary, in the case of H^+/H rich ions doped VSe_2, we observed that the additional charge carriers lead to a decrease in the conductivity of the material, due to electron doping shifting the Fermi level to higher energies and changing the band filling, in agreement with the established literature [23]. The pristine metallic behaviour observed from resistivity measurements is showing the presence of CDW transition at 93 K. We observe that the CDW behaviour is more evident after gating and the transition temperature increased in the gated sample. The gating process of 48 hours was able to induce a metal to insulator transition, increasing the resistivity of more then four orders of magnitude at low T and of one order of magnitude at high temperature. This result will be a starting point for future experiments involving longer gating time and higher gate voltage applied. Moreover, the annealing process revealed that the intercalation process is not totally stable, as a small number of intercalated ions were living the structure after the removal of gate voltage and the exposition to high T (350 K).

4.2.2 Literature results

From literature results [52] pristine VSe_2 is reported to show a **metallic behavior** with a decreasing of resistivity at the decrease of temperature. Exactly as we have seen at about 93 K in our samples, an inflection point is observed at around 70 K and it is considered the signature of a CDW transition. As a matter of fact, the presence of CDW is attested also from the study of different parameters commonly associated to **CDW phases**. In particular, VSe_2 is an appropriate candidate for magnetic-resonance study because both the vanadium and selenium nuclei are observable by NMR techniques, allowing microscopic investigation on magnetic susceptibility (χ), resistivity (ρ), and Hall constant (R), their T variation and relation with CDW phases. A unique character that distinguishes VSe_2 is that it is the only layered compound with the metal atom octaedrally coordinated with its neighbors that also possesses a low-temperature continuous CDW transition. In this respect it resembles materials as $NbSe_2$ and it shares similar features with

TaS_2 that also presents a transition to a CDW phase at low T.

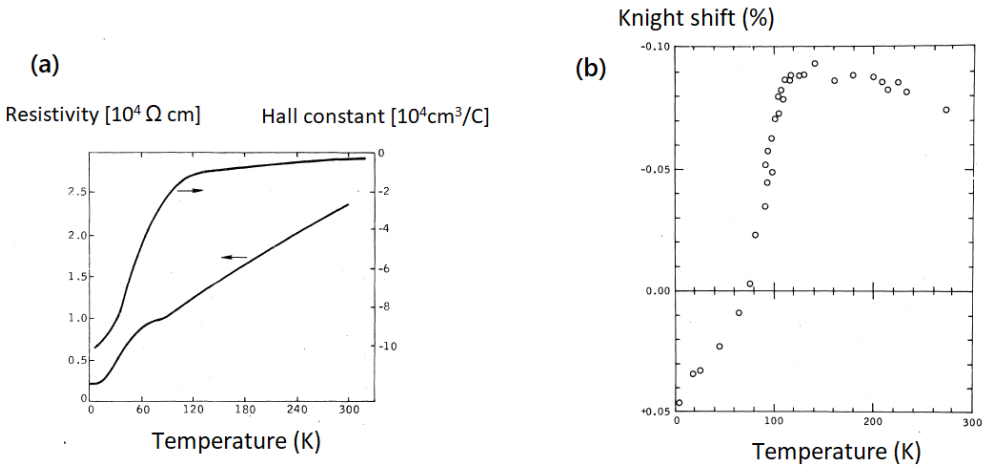

Figure 4.16: *The behavior of three measured parameters shows a peculiarity in correspondence of the CDW transition temperature [52]. (a) the behaviors of resistivity and Hall constant macroscopic parameters, revel the presence of a CDW continuous transition at low T. The resistivity decreases with temperature, with an inflection occurring in the vicinity of 70 K. Such resistivity behavior is often the signature of the onset of CDW and similar variations are observed in TaS_2. Moreover, in the dependence on T the Hall constant is negative and it increases by more than one order of magnitude at low temperatures, in the relation with CDW transition. (b) Also the Knight shift is reported here, in order to observe its variation at the onset of CDW.*

At high temperatures VSe_2 behaves as d-band metal, and Hall constant reveals the presence of different electronic charge carriers. Open questions include: the T of the peak in χ(T) often observed in VSe_2 is not related to the CDW transition temperature, and the NMR results lead to the existence of a transition near 110 K. Correlations between the various transport and magnetic properties supply definitions of CDW transition temperatures.

It is reported [53] that a special interest on VSe_2 comes from the strong electron coupling interactions for all neighboring and odd electronic configuration, that are at the origin of CDW presence. Specifically, at reduced dimensionality these are able to increase the T_C of CDW (see fig 4.17).
Monolayer 2D structures of VSe_2 show intrinsic magnetic behavior and are the first observed 2D TMD showing room temperature ferromagnetism. From exfoliation processes ultrathin structures can be obtained and the weak interactions between atomic layers suggest potential exfoliation of bulk VSe_2 into ultrathin nanosheets,

also if graphene like structures have not already been realized. In general, ultrathin nanosheets of TMD materials with single or few atomic layers, have also been studied because of their special layered structures and rich electronic properties. As a matter of fact, they are inorganic 2D materials that show similarities with graphene structure. Recently, graphene has attracted great attention due to its unique physical properties. It consists of a single layer of carbon atoms in a two-dimensional planar structure and its applications include energy storage and conversion, sensors, optoelectronic, nanoelectronic and spinelectronic devices. For these reasons, research is addressed to develop new 2D ultrathin nanoshits from TMD materials.

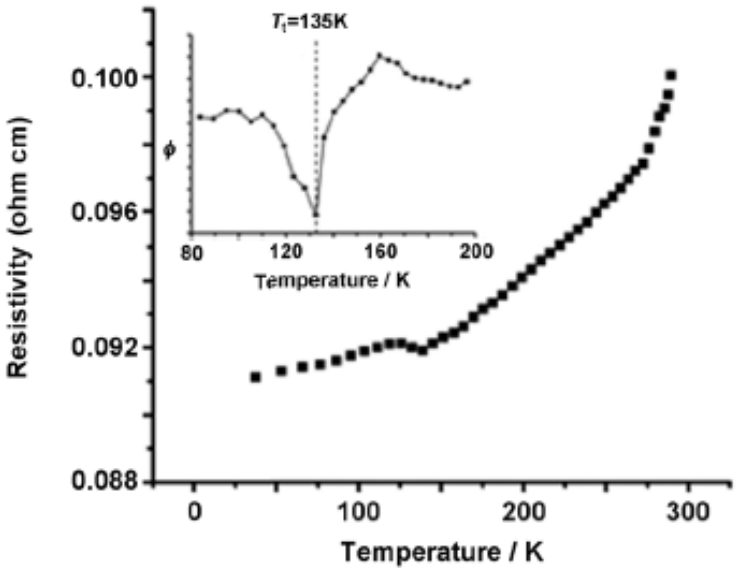

Figure 4.17: *Ultrathin nanoshits resistivity shows metallic behaviour with high T conductivity. A kink at 135 K shows CDW transition. Differently, bulk VSe_2 has T_C at 107 K [53].*

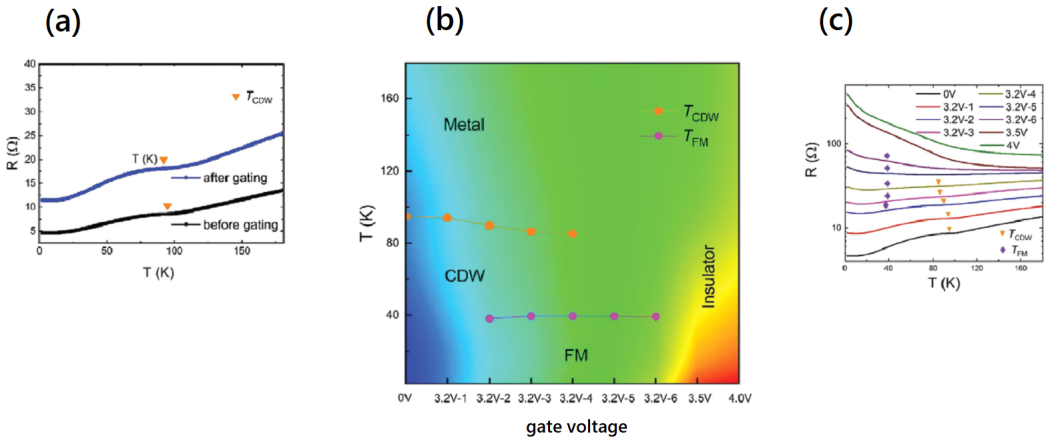

Figure 4.18: *Results on the evolution of transport properties of VSe_2 thin flakes with electric-field-driven Li-ion intercalation by using SIC-FET device [23].*

The Li-ion intercalation results can be compared with our results. As a matter of fact, the resistivity increased after the gating induced Li ions intercalation, similar to the one observed in our experiments. Zhu et al. [23] investigated the evolution of transport properties of VSe_2 thin flakes with electric-field-driven Li-ion intercalation by using SIC-FET device. The obtained temperature dependence of the resistance curve for the bulk crystal shows a metallic behaviour with a kink occurred at around 110 K corresponding to the CDW transition. Moreover, the temperature dependence of resistance of VSe_2 thin flake before and after gating show similar behaviours and identical CDW transition temperatures. The small difference of the resistance before and after gating can be supposed to be caused by the degradation of the bottom surface during the Li ions intercalation [23].

In the comparison between our results and Li-intercalation results (see Fig. 4.18, (b) and (c)), we can notice that the obtained insulating behaviours are only apparently similar between the two cases. As a matter of fact, the insulating state obtained by Li-intercalation does not show CDWs phases, and the increase of doping seems to produce a reduction in both the intensity of CDW and in the associated transition T. Differently, in our case as doping increases, the CDW behaviour is enhanced with an increase in T_{CWD}, moreover the material remains in the insulating state.

Moreover, Li-intercalated VSe_2 samples show the metal-to-insulator transition, crossing a ferromagnetic state (see Fig. 4.18, (b)). Also from our experiments, the metal-to-insulator transition is observed, so we might question whether the intermediate ferromagnetic phase is also present. Future researches will be devoted to carry out specific measurements to see if the ferromagnetic phase is also present in our case.

4.3 WSe_2. Low T Mott's VRH conduction regime

4.3.1 Our results

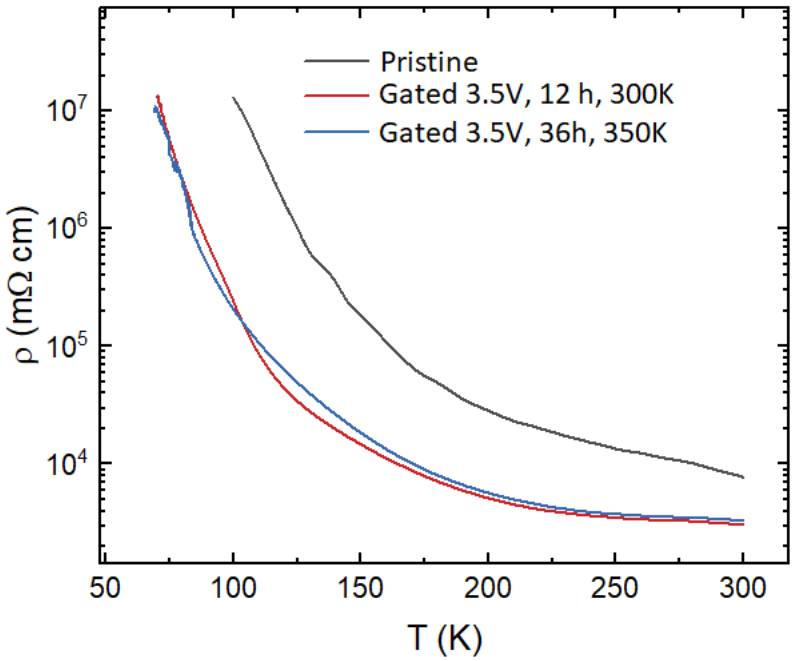

Figure 4.19: *T-dependent resistivity measurements on WSe_2.*

The Fig. 4.19 presents the results obtained from pristine and gated WSe_2 samples. The pristine sample was measured as a function of T. Then, the ionic gating technique is performed on a different sample a gate voltage of 3.5 V was applied for 12 hours, and subsequently a gate voltage of 3.5 V was applied for 36 hours at high temperature of T = 350 K. As it is presented also in literature [29] [24], WSe_2 shows a highly insulating behaviour at low T. As a consequence, the results at T < 120 K are not reliable: because the resistivity is very high compared to the low dimension of the sample, and it was not possible to measure it in a reliable way. This highly insulating behaviour is also presented in literature results (see Fig. 4.25), that reported the resistivity measurements only in the range of temperature above T = 50 K.
As it can be seen in the figure (Fig. 4.19), the observed result of H intercalation is the decrease of the resistivity level. It can be explained by the fact that the doping induced by the ionic gating process has the effect of introducing additional charge carriers into the structure and to increase its conductivity. It is assumed that an

amount of H^+ ions remains in the material after the removal of gating voltage and they induce a decrease in resistivity. Anyway, the material still remains insulating at all T.

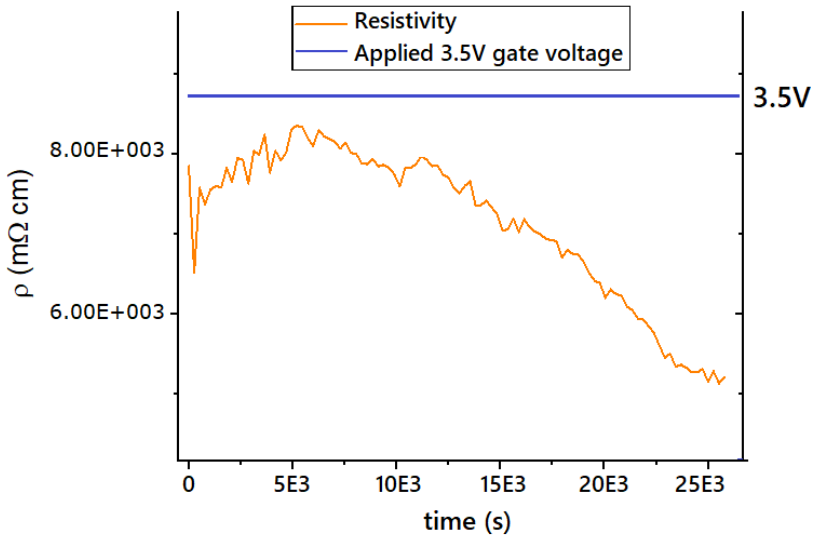

Figure 4.20: *Resistivity measurement during the ionic-gating process. The resistivity decreases during the application of a stable 3.5 V gate voltage for 12 hours.*

During the measurement of resistivity versus time, with a stable applied gate voltage of 3.5 V for 12 hours (Fig. 4.20), the resistivity decreased. The progressive reduction in resistivity suggests that the sample is evolving towards a metallic behaviour. Unfortunately, during the following T-dependent resistivity measurements it is possible to notice that the resistivity increased again after the removal of the gate voltage. This could be explained from the fact that a large amount of inserted H^+ ions had been released from the material.

Conduction regimes. Referring to the temperature dependent measurements (Fig. 4.19) it is possible to derive information about the hopping regime at the origin of the conductivity in WSe_2 samples, at the variation of T. As a matter of fact, two forms of conduction are possible in the insulating solids [54]: the thermally activated hopping from one localized state to another, or the excitation of electrons to the conduction band, which needs an activation energy ϵ. Ordered crystalline systems show well-defined electronic energy structure consisting of energy bands and energy gaps, on the contrary in the presence of disorder in the material structure, the electronic energy spectrum is described by extended and localized states,

instead of bands and gaps.
At lower temperatures, at which fewer electrons occupy the conduction bands and the most part of electrons are in localized states, the hopping electron transitions between localized states can play an essential role in the charge transport. With the decreasing of the temperature, the concentration of electrons in the conduction band decreases exponentially, and consequently their contribution to the electrical conductivity decreases. This regime is called hopping conduction. If the spatially nearest-neighbouring sites have very different energies, the probability of electron transition between these sites is very low and it is more favourable for the electron to hop to a more distant site if this site has an energy value that is closer to the initial one with respect to the nearest neighbour. This condition is called variable-range hopping (VRH). From the probability of hopping between two states separated by r distance, Mott's formula is obtained and it describes the temperature-dependent conductivity in the VRH regime:

$$\sigma = \sigma_0 \cdot \exp\left[-(T_0/T)^{\alpha}\right] \tag{4.1}$$

In order to analyse our resistivity data we plot them in the form of Arrhenius plot that displays the logarithm of conductivity $ln(\sigma)$ as a function of the inverse temperature $(1/T)^{\alpha}$.
We present on the Arrhenius plot the T-dependent resistivity measurements concerning the pristine and the doped samples. This involves the representation of the curve of $ln(\sigma)$ as a function of $T^{-\alpha}$, varying the value of α in order to find a linear dependence of the function.

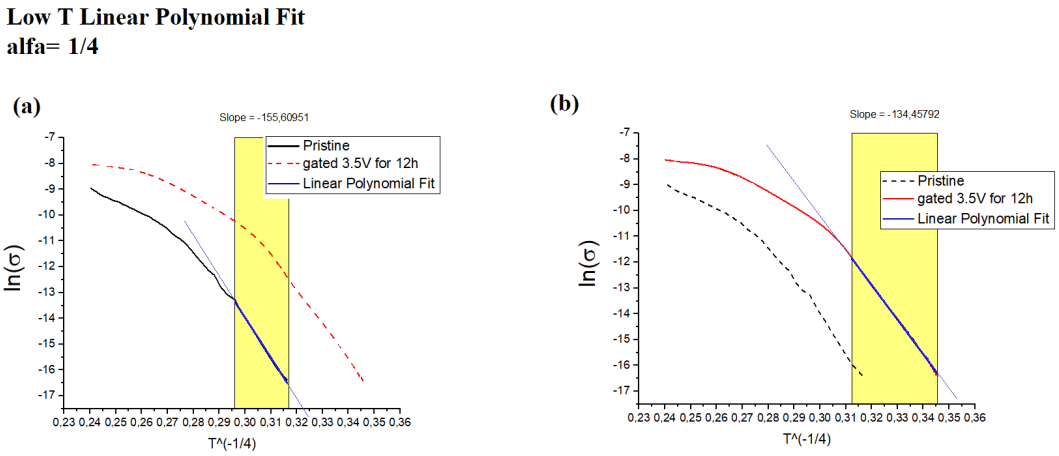

Figure 4.21: *Arrhenius plots of T-dependent resistivity measurements.*

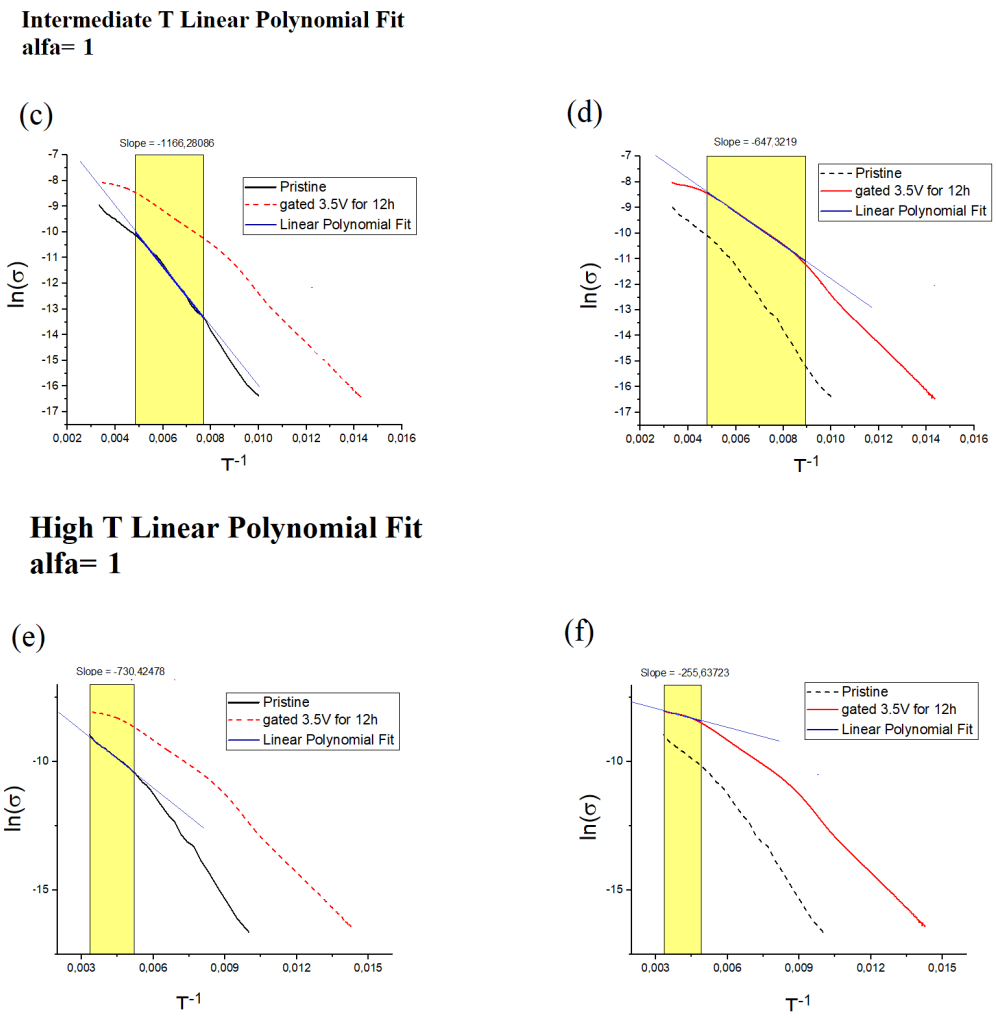

Figure 4.22: *Arrhenius plot of T-dependent resistivity measurements. The linear fit is performed on the resistivity data in three different temperature regions: low-T (a) (b), intermediate-T (c) (d) and high-T (e) (f). The plots on the left refer to the analysis on the pristine sample, the plots on the right refer to the analysis on the 12 hours gated sample.*

The Arrhenius plots of resistivity measurement is presented in Fig. 4.21 and Fig. 4.22. It presents regions with nearly linear behaviour of the function $ln(\sigma)$ vs $T^{-\alpha}$, according to different α values. As the abscissa axis reports inverse power laws of the T, the low T region are positioned in the right areas of the plots. Linear polynomial fit is performed on the functions presented in the Arrhenius plot. The graph related to the pristine case (a) and related to the 12 hours doped sample (b) shows a linear behaviour in the low T region for an exponent $\alpha = 1/4$, that refers

to Mott's 3D-VRH model. The curve related to the 36 hours gated sample was not fitted as it present constituent noise at low T.
In the low T region the linear fit is performed when imposing the exponent α = 1/4, that relates to the Mott's 3D-VRH model. So, we can deduce that the carrier transport mechanism in the temperature range between 70 K to 130 K can be described by Mott's 3D-VRH model, namely this low temperature region is dominated by the hopping mechanism of particle towards distant sites.
Differently, in the high and the intermediate T region, the analysed curves present a linear behaviour in the case of $\alpha = 1$, that refers to the Arrhenius model, which in turn can fit this range of data. Arrhenius model refers to the Nearest Neighbor Hopping (NNH) conduction regime, where the dominant behaviour of the carriers is the hopping to the nearest neighbour empty site [29].
Regarding this, we can compare our analysis with the results obtained from Kaur et al. [29] that studied the conduction mechanism at high and intermediate temperature in WSe_2 (see Fig. 4.24). In this T regions the conduction mechanisms has been described using Arrhenius model with $\alpha = 1$. The Arrhenius relation can be expressed as [55]:

$$\sigma = \sigma_0 \cdot exp\frac{E_A}{k_B T} \tag{4.2}$$

where σ_0 is a constant, E_A is the activation energy for DC (direct current) conduction, and k_B is the Boltzmann's constant. The last cited work is in accordance with our results, as it is found that a linear function fits the $ln(\sigma)$ vs T^α function in the case $\alpha = 1$, showing that thermally activated NNH conduction dominates in the high T (see Fig. 4.22(e)(f)) and intermediate T (see Fig. 4.22 (c)(d)).
Additionally, according to the different T ranges, two distinct thermal activation energies have been found in the plot for WSe_2 film, whose values are presented in the table 4.1. These values have been computed from the slopes of the linear fit of each curve, in the high and intermediate T region, using the formula: $E_A = slope/k_B$. The formula can be applied in the Arrhenius model [29].

Activation energies	Intermediate T	High T
Pristine	E_A = 844.92 meV	E_A = 529.28 meV
Doped 12 h	E_A = 469.07 meV	E_A = 185.23 meV

Table 4.1: *Activation energies (E_A) of pristine sample and 12 hours doped sample.*

We can see in our results presented in the table 4.1 that doping reduces the

activation energy because it causes a reduction in the energy-distance from the Fermi level to the conduction band, improving the thermal activated conductivity. The decreasing in the activation energy in the doped sample are in accordance with literature result obtained by Kaur et al. [29] on the carrier transport mechanism of WSe_2 in different temperature regions. The figure reported in the following literature section (see section 4.3.2) it is shown (see Fig. 4.24) that, in the temperature range from 125 K to 350 K, the carrier transport mechanism follows two different mechanisms: Mott's and Arrhenius models.
According to the physical explanation of Mott's model, it is possible to say that the carriers are localized to small states near the Fermi level, while the lower temperature region is dominated by hopping mechanism.

In summary, on this material we observed that intercalation had electron doping effect, observing an increased conductivity in the intercalated samples measurements, which increased uniformly at all T. The increase in gating time did not affect the decrease in resistance proportionally: by increasing the gating time from 12 hours to 36 hours, the obtained curves of resistivity versus temperature were similar. Also the gating process performed at high T of 350 K, did not give a stabilization of the level of charge obtained during gating; on the contrary, this process was able to stabilize the intercalation level in TaS_2 structure (see section 4.1).
Observing the behaviour of the resistivity curve versus time, during the application of a stable gate voltage, the resistivity decreases considerably. So, the gating appeared to be able to introduce H^+ rich molecules into the sample, until evolving its electronic properties towards the metallic state but without reaching a sufficient doping level to trigger the insulator-to-metal transition.

As we will see in detail in the next paragraphs, different methods have been successfully applied on WSe_2, obtaining a large increase in conductivity which was accompanied by the semiconductor-metal transition. It is possible to cite, intercalation of potassium [20], application of pressure [56] and thickness reduction [57]. In addition, WSe_2 integrated on graphene structures [58] was shown to stabilize the transition to the superconductive state of the latter.

4.3.2 Literature results

In a general overview from literature we can report that Tungsten (W) has a relatively high atomic number and its compounds are in the family of commonly employed TMDs. It has a relatively large charge, with respect to other elements. As a consequence, it gives the opportunity for the formation of spacious interlayer channels and promotes the formation of large hexagonal structures. Moreover, it provides a good flexibility for doping, since the difference in size of the dopant,

compared with the substituted element, is an important factor. Hence, it is easier to replace larger atoms with smaller atoms [18].

It provides good electrical conductivity, which is critically important for energy storage, optoelectronics and magnetic applications. Moreover, selenium (Se) is considerably cheap, while it has high electrical conductivity. It is noticeable that in heavy TMD compounds the interaction energy between molecules decreases for heavier chalcogens, due to the longer distance between the metal atoms. This feature can be exploited, as it provides a better opportunity to alter the 2D structure with the possibility of introducing charge and dopant in the large interlayer space, in order to control the materials properties [18].

Comparison with molybdenum (Mo). A largely studied TMDs is MoS_2, due to the possibility of obtaining a 2D structure. Tungsten dichalcogenides have recently attracted the attention because of W high atomic number, that is larger then Mo, which related features can be exploited to alter the 2D structure. This alteration may result in opening new opportunities. W natural abundance is higher in the Earth's crust if compared to Mo, and it is also less toxic [59]. Also, the industrial consumption of Mo is currently higher while having a lower amount of mineral resources [18]. For this reason, WS_2 and WSe_2 have recently attracted considerable attention. Consequently, W-based TMDs are normally considered as an alternative to Mo counterparts and W can be commercially more favourable for future industrial applications, such as in the field of energy storage and conversion (e.g. solar panels), or of sensors and biosensors [24].

Doping and pressure in W based structures. Computational studies suggested that metal behaviour can be induced in WS_2 monolayers by introducing dopants into the lattice structure. Moreover, it has been showed that the application of pressure allows the semiconducting structure of WS_2 to undergo metallic transition and this is due to the overlap of the highest valence band with the lowest conduction band [56]. WSe_2 can host n and p types doping, and it has a tendency towards p-type doping. The current method is to chemically facilitate the doping by oxidising or reducing agents having appropriate redox potential. In this context, we remember that p-type doping is the insertion of acceptor dopant molecules in the sample structure that adds positive conductive charges in the structure. On the contrary, n-type doping is the insertion of donor dopant molecules that adds negative conductive charges [60].

Doping can have the consequence of directly redistributing the charge over the 2D structure of TMDs. Moreover, also metallic impurities can interact with the Se atoms to affect the charge distribution over the WSe_2 lattice and this mechanism can act like doping [61].

A used technique is to mix two different tungsten dichalcogenides: in this case,

one chalcogen will serve as a dopant in the dominant structure. Owing to the similarity of chalcogens structure, the resulting architecture is subject to a uniform deformation. This led to a distribution of the charge over the TMD structure that can be suitable for applications [62].

Superconductivity in graphene stabilized by WSe_2. A research [58] reports that WSe_2 may play an essential role in enhancing the superconductive behavior in metallic twisted bilayer graphene structure stabilized by WSe_2. As a matter of fact, twisted bilayer graphene (TBG) band diagram shows flat electronic bands which can host a rich phase diagram of insulating, superconducting, ferromagnetic and topological phases, when inserted in a more complex structure. At this purpose, correlated insulator structures made of hexagonal boron nitride (hBN) are used to encapsulate the graphene sheets and this structure shows the importance of the microscopic dielectric environment. In our context is interesting the fact that adding an insulating WSe_2 monolayer between the hBN and the TBG plays a role in stabilizing the superconductivity. Devices made from hBN–TBG–WSe_2–hBN stacked togheter by van der Waals forces have been investigated, in which a monolayer of WSe_2 is placed between the hBN and TBG (Fig. 4.23).

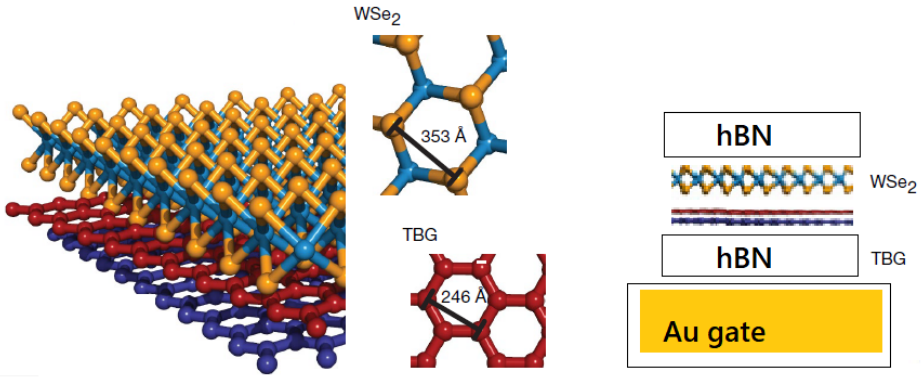

Figure 4.23: *Superconductivity observed in TBG–WSe_2 structures. The schematic representation (on the left) of the TBG–WSe_2 structure is showing the crystal lattice of the two graphene layers (red and blue) and WSe_2 (yellow and cyan). In the central image the different unit-cell sizes of TGB and WSe_2 are indicated. The image on the right shows the complete structure, including the encapsulating insulating hBN layers on the top and on the bottom [58].*

In the context of WSe_2 **intercalation**, spectroscopic measurements [20] reported the electron energy-loss of potassium (K) intercalation on WSe_2. Pristine WSe_2 films were exposed to potassium and the result involved charge carrier plasmon

excitation observed at 0.97 meV. This can indicate a **semiconductor-to-metal transition** as a consequence of potassium addition.

Moreover, it is reported [63] that Cesium (Cs) doping has been employed to obtain n-type (electron doped) WSe_2 transistors. Specifically the doping allowed to reduce contact resistance as it induced a semiconductor to metal (from 2H to 1T' polytypes) phase transition and the monitored electron mobility was enhanced by nearly 50 times.

Finally, it is possible to report here some relevant literature results that can be compared to our results and analysis, at this purpose the Fig. 4.25 confirms a similar trend of T-dependent resistivity obtained in WSe_2 thin films at the variation of sample thicknesses. As in our case the resistivity was measured for T > 125 K, as the sample showed a highly insulating behaviour at lower T that doesn't allow to properly measure its high resistivity values. The analysis of conductive regimes are discussed in Fig. 4.24.

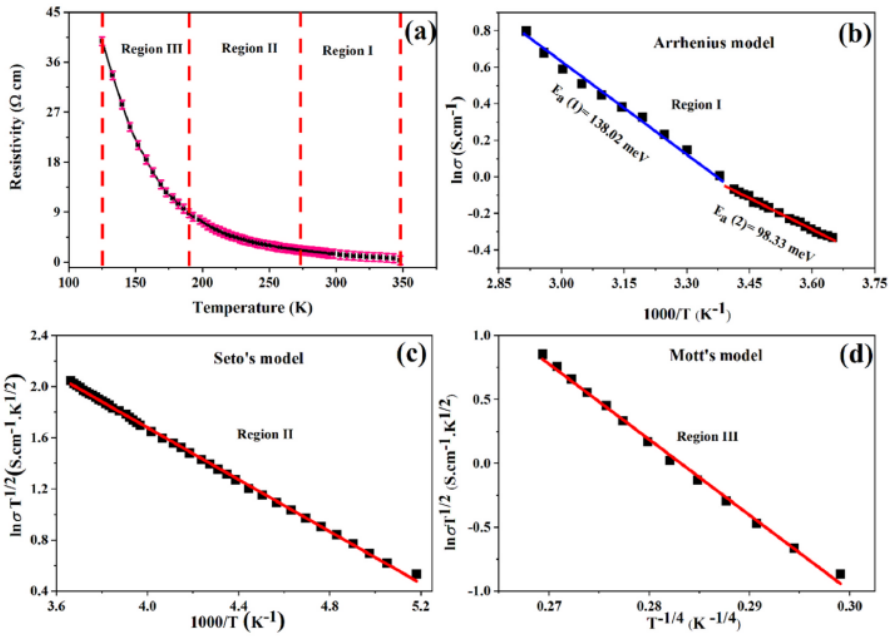

Figure 4.24: *a) The resistivity of WSe_2 thin films as a function of temperature (range 125 K – 350 K). The different T regions have been fitted with different models. (b) Arrhenius model fits on the conductivity data in the temperature range 350 – 273 K. (d) Mott's VRH model fits on the conductivity data in the temperature range 190 K – 125 K [29].*

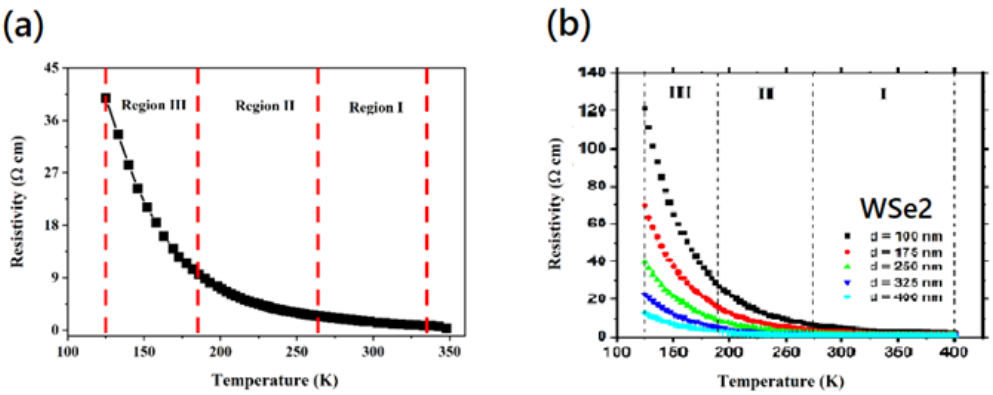

Figure 4.25: *The temperature-dependent electrical properties has been analyzed of fabricated thin films. The figure (a) shows the resistivity variation with temperature for the WSe_2 film in the temperature range from 125 K to 348 K. There is a decrease in resistivity with the increases in temperature which shows the semiconducting behaviour of deposited WSe_2 film. The three different regions in the resistivity plot with temperature indicate that there may be more than one carrier transport mechanisms involved in WSe_2 film [29]. (b) Thickness dependent results of 2D WSe_2 thin films on glass substrate. The thickness of the WSe_2 films was varied from 100 μm to 400 μm [24].*

4.4 $NiTe_2$: a type-II Dirac semimetal

4.4.1 Our results

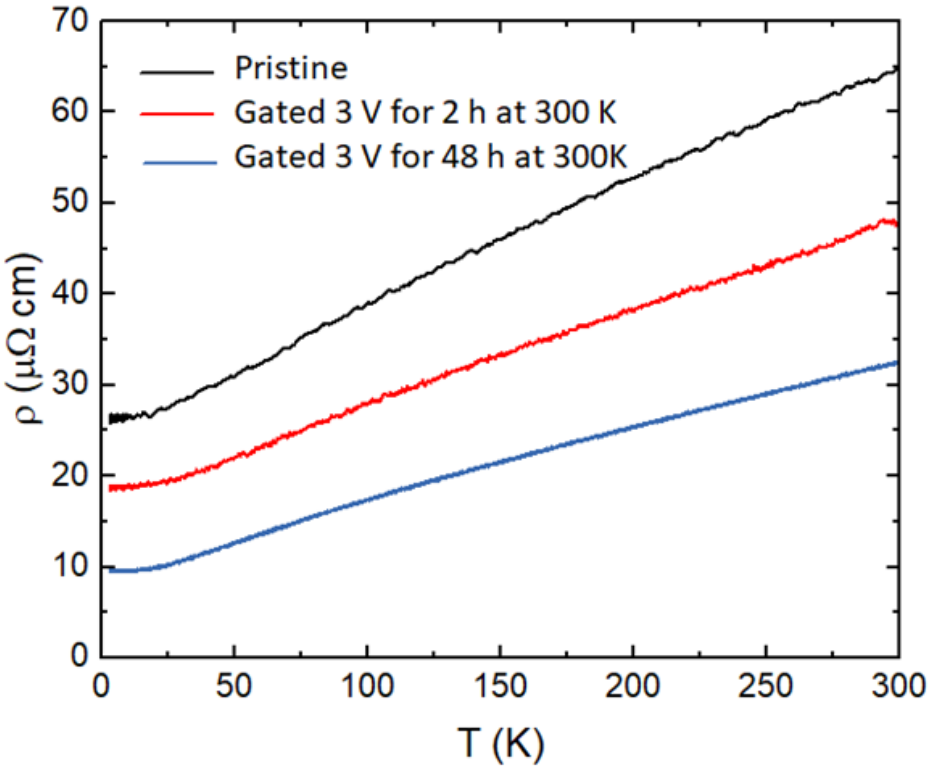

Figure 4.26: *Resistivity versus temperature of $NiTe_2$ from cryocooler measurements. The trend of the curves of the pristine and gated samples are very similar, while the curve values decrease as the increase of gating level.*

The resistivity of $NiTe_2$ was measured in the van der Pauw configuration on the same sample in different phases related to different levels of intercalation. The thickness of the sample was ≈ 40 μm and it remained stable after the intercalation, thus suggesting that here most of the doping is related to the intercalation of H^+ ions. The pristine sample was measured as a function of temperature. Then, a first gating process was performed: a gate voltage of 3 V was applied for 2 hours, and the resistivity of the doped sample was measured with respect to temperature. A second gating process was performed: a gate voltage of 3 V was applied for 2 days and the resistivity versus temperature was measured again. As it is presented in Fig. 4.26, the resistivity curve for the pristine and doped samples had a similar

behaviour, the differences being mainly related to the decrease in the resistivity observed in the doped samples. Namely, the addition of H^+ induced a lower level of resistivity with a similar behavior of the curve. As we already said, in this case we didn't observe an increase in the thickness of the samples after gating; for this reason we can say that the gating induced the insertion of H^+ ions in the sample structure and not of larger molecules

The resistivity of intercalated samples almost reflected the pristine values rescaled by a constant, except for the behaviour at the highest doping and at low temperature. In this case (blue curve in Fig. 4.19 and 4.20), at low temperature there is an increasing in the slope in the resistivity of the doped samples.
The difference between the slopes can be better observed in the normalized curves (see Fig. 4.27) and this indicates a slight change in the residual resistivity ratio. We remember that the residual-resistivity ratio is defined as the ratio of the resistivity of a material at room temperature (300 K) and at low temperature.

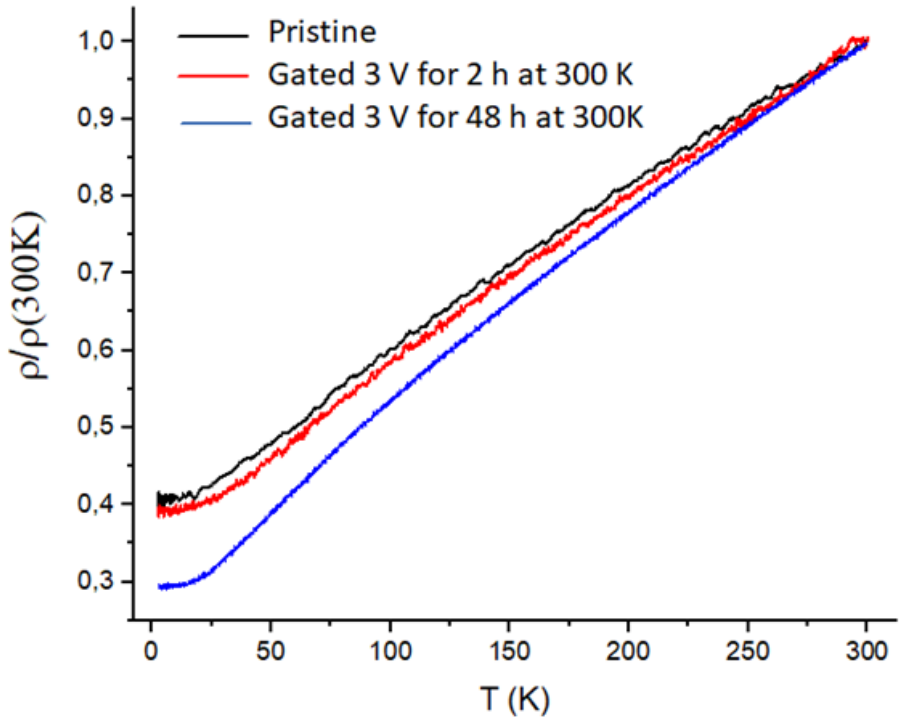

Figure 4.27: *Normalized curves of $NiTe_2$ resistivity with respect to their value at 300 K.*

When we normalize the three curves with respect to the resistivity at 300 K

is calculated we can see that the three normalized curves are almost overlapping. A slight difference in the slope is observed on the most-doped sample: the blue curve, corresponding to the sample doped for 48 hours, drops with an increased slope with respect to the curve of the pristine sample (black curve). To get more information regarding this feature, the values of the residual resistivity ratio (RRR) are measured on the three curves. It should be noted that here the definition of RRR is $\rho(300K)/\rho(2.8K)$: the ratio of the resistivity of a material at room temperature and at 2.8 K [64]. The computed values are: 2.46 for the pristine, 2.55 for the 2 hours doped sample and 3.37 for the 48 hours doped sample. This shows an increase of RRR for the doped sample with respect to the pristine sample, in particular a more relevant difference is observed between the pristine and the highest doped sample. From the results of the resistivity measurement, it can be deduced that the main effect of H doping is to increase the amount of electron charge in the structure, which causes the conductivity of the sample to increase, and thus the resistivity to decrease.
During the gating process additional H^+ ions are inserted and consequently the total electron charge is increased in the sample structure.

$$\sigma = \frac{ne^2\tau}{m} \tag{4.3}$$

In Drude formula (see Eq. 4.3): σ is the conductivity (the inverse value of resistivity), n is the number of charge carriers per unit volume, τ is the mean free time between electron collisions, m is the effective mass of the electron, e is the charge of the electron.
Referring to Drude's formula of conductivity, we can say that the effect of doping on the decrease of the resistivity value depends mainly on the increasing of n in the formula and the metallic behavior of the material is enhanced as the doping level increases.
As we already reported, there is a higher slope in the doped cases compared to the pristine case and this fact could be related to a decrease in the disorder in the structure because of gating. In the specific, the reason of the increasing in the slope, could be related to different factors. At the fundamental level of solid state physics [64], in a crystal lattice, electrons can scatter with defects in the lattice or with lattice vibrations. Deriving from these two factors, the total ρ is the sum of ρ_0 at low T, which is due to the disorder produced by defects, impurities and dislocations, and $\rho(T)$, which is due to electron-phonon scattering. Consequently, the increase of the slope in the doped samples, can be due to the two different contributions:

1. An improved electronic screening increases the mobility, $\mu = e \cdot \frac{\tau}{m}$, because it reduces the influence of defects and lattice vibrations on the electron behaviour.

So, there is a decreasing in the residual resistivity ratio. In this case, the level of disorder in the system is reduced, because of the more efficient screening.

2. The level of disorder remains approximately the same, and the electron-phonon coupling increases because of doping.

When both ρ_0 and ρ(T) are decreasing (as shown in Fig. 4.26) there are two distinct ways for the RRR to increase: either ρ_0 decreases more than $\rho(T)$, or $\rho(T)$ decreases less than the residual resistivity. Thus, it turns out that the experimental findings can results from a combination of both the afore mentioned effects.

The only way to understand the role of these contributions is to measure the temperature dependence of the carrier density performing Hall effect measurements, and to combine it with the temperature dependence of the resistivity. This allows to determine the values of the mobility as a function of temperature. The role of the doping can be associated to an relevant increase in the screening effect.
For this reason, future research can include the measurement of Hall effect to determine the type, the number and the properties of the charge carriers in our protonated $NiTe_2$ samples. This would allow to understand more about the factors that influence the resistivity behaviour and the role of H doping on the mobility.

In summary, in $NiTe_2$ the metallic behavior was enhanced by H insertion that has an electron-doping effect and produces an almost uniform increase in conductivity at all T. An additional feature is observed in the slight increase of the resistivity slope of gated sample. The reason of this increase in the RRR could be ascribed to a possible reduction of the disorder in the intercalated sample at low T due to an improved screening of the mobile charge carriers, to an increase of the electron-phonon coupling or to a mixing of these two effects.

4.4.2 Literature results

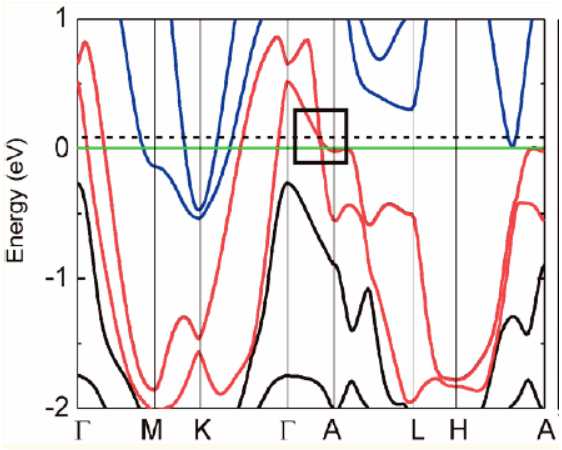

Figure 4.28: *The type II Dirac point is visible on the band diagram of $NiTe_2$ [65]*

Type-II Dirac semimetal. Nickel ditelluride ($NiTe_2$) is a recently discovered Type-II Dirac semimetals with topological Dirac fermions near the Fermi energy. Considering Ni based TMDs, $NiTe_2$ has been the most studied as it shows unusual phenomena both in bulk and at reduced dimension. Thickness-mediated electronic tunability and pristine two-gap superconductivity in the single-layer limit are significant features observed in the context of $NiTe_2$ research [66]. Two-gap superconductivity can be found when two superconducting gaps of different sizes reside on different disconnected regions of the Fermi surface [67]. For this purpose, different works reported the spectroscopic evidence for the dimensionality crossover of single-crystalline ultrathin $NiTe_2$ films as a function of film thickness. Namely, as the film thickness increases from one to five layers, the gap closes. On the pristine material, two-gap superconducting state has been observed in single-layer $NiTe_2$ with $T_C \approx 5.7$ K. Also bilayer $NiTe_2$ intercalated with an alkali metal has the possibility to be a two-gap superconductor [66]. However, the difficulties in the fabrication of $NiTe_2$ monolayer or bilayer flakes limit the possibility of device applications.

Electronic band diagram measurements [66] shows $NiTe_2$ to be a type-II Dirac semimetal, in which low-energy excitations of the Dirac fermions generate a tilted Dirac cone, as it can be seen on the band diagram in the figure (Fig. 4.28). In particular, such symmetry breaking could generate electronic and physical properties that distiguish $NiTe_2$ from other topological semimetals, such as the potential presence of unconventional superconductivity, anisotropic magnetoresistance and chirality. Relevant results [66] came from $NiTe_2$ flakes of triatomic layers that are

fabricated using molecular beam epitaxy on bilayer graphene surfaces. Results relate to the appearance of linear bands near the Fermi level attributable to the lower branches of the type-II Dirac limit cone that are present in the bulk. The interest comes from the dimensionality crossover from the ultrathin-film to bulk-like regimes.

We already said that type-II Dirac fermions manifest themselves as strongly tilted Dirac cones [68], where an electron and a hole-like Fermi surfaces touch at the energy of the Dirac point. Assuming that the Dirac point is in the vicinity of the Fermi level, type-I and type-II Dirac fermions display distinct physical properties. Many properties originate from the fact that the density of states at the Dirac node is vanishing for type I, while it is finite for type-II Dirac fermions.
Recently, type-I Dirac fermions near E_F have been identified in a variety of different systems, as for example in graphene or high-temperature iron-based superconductors [69], while type-II Dirac fermions seem to be much less common. Their existence has been predicted theoretically in TMD semimetals as a new state of quantum matter showing different behavior with respect to type I Dirac fermions. It has been reported [70] that in $NiTe_2$, a pair of type-II Dirac nodes are located very close to the Fermi level and the type-II Dirac cone can be tuned to E_F by chemical substitution. $NiTe_2$ represents a suitable platform to study the type-II Dirac physics from transport and thermodynamic measurements [21]. The theoretical understanding of quantum oscillations associated with the Dirac fermions would possibly facilitate the applications based on these topological carriers [70].

Pressure induced superconductivity. It is reported [26] that $NiTe_2$ under pressure has shown the onset of superconductivity with a transition temperature of $T_C \approx 7.5$ K. Recent reports of pressure-induced superconductivity in a variety of topological materials have motivated the exploration of possible SC in $NiTe_2$ associated with electronic topological transition (the Lifshitz transition).

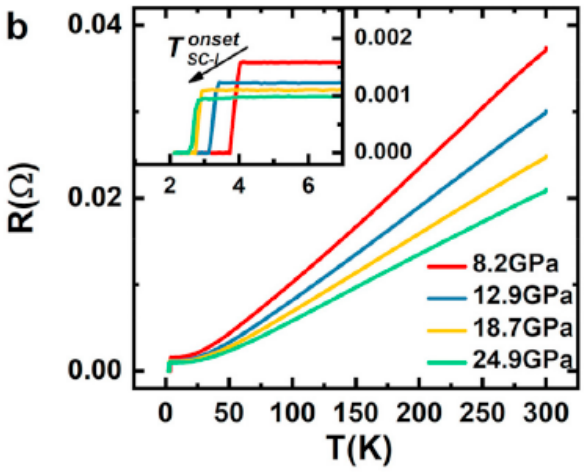

Figure 4.29: *Resistivity curves are reported as a function of T for 2 < T < 300 K and different applied pressures of P = 8.1, 12.9, 18.7 and 24.9 GPa. When pressure increases, the SC transition temperatures T_C decreases [26].*

Te vacancies. Feng et al. [26] report relevant experimental evidences for pressure-induced superconductivity in non-stoichiometric Te deficient samples: $NiTe_{2-x}$ (x = 0.38) single crystals. The pristine state properties of Te-deficient $NiTe_{2-x}$ exhibit relevant differences from $NiTe_2$. The two pressure-dependent superconducting phases are correlated with two different crystalline structures: the typical hexagonal structure of $NiTe_2$ becomes monoclinic in the case of Te-deficient sample ($NiTe_{2-x}$). The studies of various pressure-dependent properties suggest that Te vacancies in $NiTe_{2-x}$ play an important role in the structural and electronic properties as well as the appearance of two-phase SC (see next paragraph). Also, the wide pressure range is promising for further investigation of topological SC [26].

In the same research work, pressure-induced two-phase superconductivity (type I and type II SC) was found, with a maximum $T_C = 7.8K$. Type I SC phase was associated with the hole-dominant $NiTe_2$ one, while type II SC phase was related to the electron-dominant $NiTe$ phase. Moreover, a different temperature dependence of the upper critical fields for the two SC phases is observed.
The Dirac point closest to the Fermi level (E_F) of $NiTe_2$ was found to shift with pressure, from below E_F in the hexagonal phase, to above E_F in the monoclinic phase. In conclusion, the actual discoveries around $NiTe_2$ showed the role of modifying TMDs by introducing vacancies and applying pressure to achieve new structural and electronic phases.

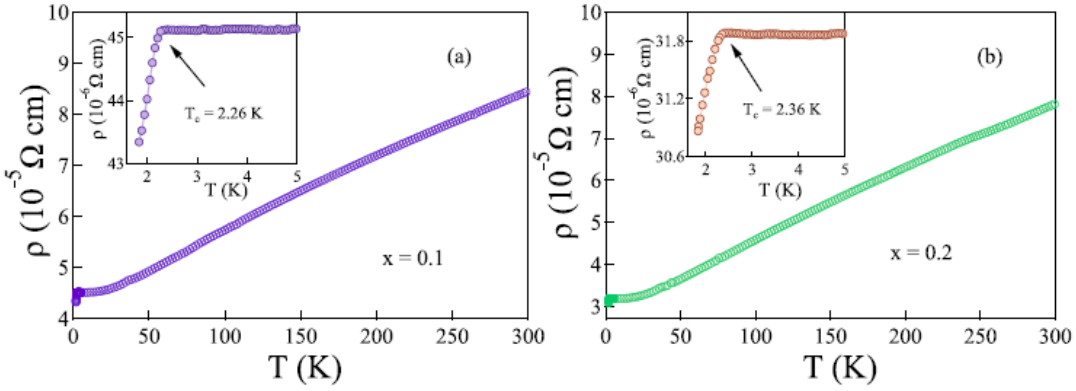

Figure 4.30: *Temperature dependence of resistivity for $Ni_{1x}Re_xTe_2$ with $x = 0.1$ (a) and $x = 0.2$ (b). The inset shows the drop of resistivity at $T_C = 2.26K$ and $T_C = 2.36K$ respectively [21].*

Re doping. A series of layered $Ni_{1x}Re_xTe_2$ crystals have been realized [21] with x varying from 0 to 0.20. In Fig. 4.30 results are reported. Pristine bulk $NiTe_2$ crystal is not known to be a SC. Magnetic and transport measurements highlighted that Re substitution in Ni sites induced superconductivity acting as hole-doping. The main results demonstrated that $Ni_{1x}Re_xTe_2$ samples (x = 0.1 and x = 0.2) display type-II superconductivity respectively at T_C = 2.3 K and T_C = 2.4 K, with higher critical field H_C of 0.92 and 0.97 T. Moreover, in the relation with SC behavior, the specific heat measurements affirmed that the electron-phonon coupling constant and the density of states increases with the increment of Re content, favouring SC conditions. Evidence for hole-like charge carriers has been illustrated by Hall effect measurements in Re doped sample, differently from the undoped compound, where electrons are the main charge carriers. The estimated values of the Debye temperature, θ_D is an indicator of the phonon softening in the lattice at the introduction of Re doping, this feature is consistent with hole-doped superconductivity. Hole-doped systems in 2D van der Waals layered materials are interesting candidates as 2D superconductors [21].

Chapter 5

Conclusions

This thesis work is set in the context of researches focused on the discovery of high-temperature superconductivity under ambient pressure conditions, investigating the right combination of techniques and materials. The original aim of the project was to attain hydrogen-induced superconductivity in selected layered compounds. While this goal has not yet been attained, this thesis work was successful in tuning the metallic and insulating phases of four TMDs materials, by means of ionic-gate-induced intercalation of hydrogen and hydrogen-rich ions. The main results obtained from each sample can be summarized as follows.

From our experiments on 1T-TaS_2, we can conclude that the most successful result derived from the high T = 350 K gating process. It was able to increase the conductivity of the sample and additionally the dopant content in the structure revealed not to be volatile. The structure was stable for long time and also it remained stable when exposed to annealing at high T. For this reason, future experiments can involve high T performed gating processes, imposing longer gating periods, and imposing higher values of gate voltage. The purpose is to find the best combination of the parameters affecting gating process: including voltage, time and temperature.

In the case of H-doped VSe_2, we observed that the additional charge carriers lead to a decrease in the conductivity of the material in agreement with the established literature. The pristine metallic behaviour observed from resistivity measurements is showing the presence of CDW transition at 93 K. We observe that the CDW behaviour is more evident after gating and the transition temperature increased in the gated sample with respect to pristine the sample. The gating process of 48 hours was able to induce a metal-to-insulator transition, increasing the resistivity of four orders of magnitude at low T and of one order

of magnitude at room temperature. This result will be a starting point for future experiments involving longer gating time and higher gate voltage applied. Moreover, the measurement after the annealing process revealed that the intercalation process is not totally stable, as an amount of intercalated ions were living the structure after the removal of gate voltage and the exposition to high T (350 K).

In $NiTe_2$, the metallic behavior was enhanced by H insertion that has electron doping effect. As a matter of fact, it involved an almost uniform increase in conductivity at all T. An additional feature is observed in the slight increase of the resistivity slope of gated sample. The reason of this slight increase of the residual resistivity ratio (RRR) in the most doped sample, could be related to the presence of an interesting effect due to the increase in charge carrier density, that can lead to an increase in screening (with a consequent decrease in the disorder of the electronic system) or to an increase in electron-phonon coupling.

From WSe_2 measurements, we observed that intercalation had electron doping effect, observing an increased conductivity in the intercalated samples measurements, which increased uniformly at all T. The increase in gating time did not affect the decrease in resistance proportionally: by increasing the gating time from 12 hours to 36 hours, the obtained curves of resistivity versus temperature were similar. Observing the behaviour of the resistivity curve versus time, during the application of a stable gate voltage, the resistivity decreases considerably. So, the gating appeared to be able to introduce electron donors into the sample, evolving its electronic properties towards a metallic state, but not being sufficient to actually attain an insulator-to-metal transition.

No samples presented the transition to the superconducting state. However, the effects observed on the behavior of the intercalated structures are promising. Further research can be devoted to the implementations of H intercalation by ionic-gating technique.

Bibliography

[1] D Garfias. «Applied Superconductivity in Current and Emerging Technologies». In: *Team Energy* () (cit. on p. 2).

[2] AP Drozdov et al. «Superconductivity at 250 K in lanthanum hydride under high pressures». In: *Nature* 569.7757 (2019), pp. 528–531 (cit. on p. 1).

[3] L Boeri et al. «The 2021 room-temperature superconductivity roadmap». In: *Journal of Physics: Condensed Matter* 34.18 (2022), p. 183002 (cit. on p. 1).

[4] T Ritschel, J Trinckauf, G Garbarino, M Hanfland, M v Zimmermann, H Berger, B Büchner, and J Geck. «Pressure dependence of the charge density wave in 1 T-TaS 2 and its relation to superconductivity». In: *Physical Review B* 87.12 (2013), p. 125135 (cit. on pp. 2, 9, 33, 36–38).

[5] LJ Li, WJ Lu, XD Zhu, LS Ling, Z Qu, and YP Sun. «Fe-doping–induced superconductivity in the charge-density-wave system 1T-TaS2». In: *EPL (Europhysics Letters)* 97.6 (2012), p. 67005 (cit. on pp. 2, 9, 33, 34, 37).

[6] Y Meng et al. «Protonation-induced discrete superconducting phases in bulk FeSe single crystals». In: *Physical Review B* 105.13 (2022), p. 134506 (cit. on pp. 2, 3, 14).

[7] M Chhowalla, Z Liu, and H Zhang. «Two-dimensional transition metal dichalcogenide (TMD) nanosheets». In: *Chemical Society Reviews* 44.9 (2015), pp. 2584–2586 (cit. on pp. 2, 6, 11).

[8] M Yoshida, Y Zhang, J Ye, R Suzuki, Y Imai, S Kimura, A Fujiwara, and Y Iwasa. «Controlling charge-density-wave states in nano-thick crystals of 1T-TaS2». In: *Scientific reports* 4.1 (2014), pp. 1–5 (cit. on pp. 2, 9, 10, 33, 34, 36).

[9] RS Gonnelli, E Piatti, D Romanin, and D Daghero. «20. Is protonation (hydrogenation) the future of conventional superconductivity at room pressure?» In: *The 2021 Room-Temperature Superconductivity Roadmap* () (cit. on pp. 2–5).

[10] Y Cui et al. «Ionic-liquid-gating induced protonation and superconductivity in FeSe, FeSe0. 93S0. 07, ZrNCl, 1T-TaS2 and Bi2Se3». In: *Chinese Physics Letters* 36.7 (2019), p. 077401 (cit. on pp. 2, 3, 13, 14, 32).

[11] E Piatti, D De Fazio, D Daghero, SR Tamalampudi, D Yoon, A Ferrari, and RS Gonnelli. «Multi-valley superconductivity in ion-gated MoS2 layers». In: *Nano letters* 18.8 (2018), pp. 4821–4830 (cit. on pp. 3, 4, 7).

[12] GE Volovik. «Topological lifshitz transitions». In: *Low Temperature Physics* 43.1 (2017), pp. 47–55 (cit. on p. 5).

[13] SA Han, R Bhatia, and S Kim. «Synthesis, properties and potential applications of two-dimensional transition metal dichalcogenides». In: *Nano Convergence* 2.1 (2015), pp. 1–14 (cit. on p. 6).

[14] RA Klemm. «Pristine and intercalated transition metal dichalcogenide superconductors». In: *Physica C: Superconductivity and its Applications* 514 (2015), pp. 86–94 (cit. on pp. 7, 9, 13).

[15] A Eftekhari. «Tungsten dichalcogenides (WS 2, WSe 2, and WTe 2): materials chemistry and applications». In: *Journal of Materials Chemistry A* 5.35 (2017), pp. 18299–18325 (cit. on pp. 7, 8).

[16] RA Klemm. «Striking similarities between the pseudogap phenomena in cuprates and in layered organic and dichalcogenide superconductors». In: *Physica C: Superconductivity* 341 (2000), pp. 839–842 (cit. on pp. 7, 8, 11, 12).

[17] T Timusk and B Statt. «The pseudogap in high-temperature superconductors: an experimental survey». In: *Reports on Progress in Physics* 62.1 (1999), p. 61 (cit. on p. 8).

[18] L Gan, Q Zhang, Y Zhao, Y Cheng, and U Schwingenschlögl. «Order-disorder phase transitions in the two-dimensional semiconducting transition metal dichalcogenide alloys Mo1- xWxX2 (X= S, Se and Te)». In: *Scientific reports* 4.1 (2014), pp. 1–5 (cit. on pp. 8, 54).

[19] Jl A Wilson, FJ Di Salvo, and S Mahajan. «Charge-density waves and superlattices in the metallic layered transition metal dichalcogenides». In: *Advances in Physics* 24.2 (1975), pp. 117–201 (cit. on p. 8).

[20] M Ahmad, E Müller, C Habenicht, R Schuster, M Knupfer, and B Büchner. «Semiconductor-to-metal transition in the bulk of WSe2 upon potassium intercalation». In: *Journal of Physics: Condensed Matter* 29.16 (2017), p. 165502 (cit. on pp. 9, 53, 55).

[21] M Mandal and RP Singh. «Emergent superconductivity by Re doping in type-II Weyl semimetal NiTe2». In: *Journal of Physics: Condensed Matter* 33.13 (2021), p. 135602 (cit. on pp. 9, 63, 65).

[22] Y Yu et al. «Gate-tunable phase transitions in thin flakes of 1T-TaS2». In: *Nature nanotechnology* 10.3 (2015), pp. 270–276 (cit. on pp. 9, 33–35).

[23] C Zhu, B Lei, F Meng, J Cui, W Zhuo, W Wang, Z Xiang, and X Chen. «Realizing Ferromagnetism in a Field-Effect Transistor Based on VSe2 Thin Flakes». In: *Advanced Electronic Materials* (2022), p. 2101383 (cit. on pp. 9, 44, 47).

[24] M Alzaid, NMA Hadia, ER Shaaban, M El-Hagary, and WS Mohamed. «Thickness controlling bandgap energy, refractive index and electrical conduction mechanism of 2D Tungsten Diselenide (WSe2) thin films for photovoltaic applications». In: *Applied Physics A* 128.2 (2022), pp. 1–12 (cit. on pp. 9, 48, 54, 57).

[25] Q Dong et al. «Structural phase transition and superconductivity hierarchy in 1T-TaS2 under pressure up to 100 GPa». In: *npj Quantum Materials* 6.1 (2021), pp. 1–7 (cit. on pp. 9, 36).

[26] Z Feng et al. «Evidences for pressure-induced two-phase superconductivity and mixed structures of NiTe2 and NiTe in type-II Dirac semimetal NiTe2-x (x= 0.38±0.09) single crystals». In: *Materials Today Physics* 17 (2021), p. 100339 (cit. on pp. 9, 63, 64).

[27] LJ Li, WJ Lu, Y Liu, Z Qu, LS Ling, and YP Sun. «Influence of defects on charge–density–wave and superconductivity in 1T-TaS2 and 2H-TaS2 systems». In: *Physica C: Superconductivity* 492 (2013), pp. 64–67 (cit. on pp. 9, 33, 38).

[28] X Huang, C Liu, and P Zhou. «2D semiconductors for specific electronic applications: from device to system». In: *npj 2D Materials and Applications* 6.1 (2022), pp. 1–19 (cit. on p. 9).

[29] M Kaur, K Singh, I Chauhan, H Singh, RK Sharma, A Vij, A Thakur, and A Kumar. «Low temperature carrier transport mechanism and photoconductivity of WSe2». In: *Journal of Alloys and Compounds* 869 (2021), p. 159369 (cit. on pp. 9, 48, 52, 53, 56, 57).

[30] RE Thorne. «Charge-density-wave conductors.» In: *Physics Today* 49.5 (1996), pp. 42–47 (cit. on p. 9).

[31] MD Johannes and II Mazin. «Fermi surface nesting and the origin of charge density waves in metals». In: *Physical Review B* 77.16 (2008), p. 165135 (cit. on p. 10).

[32] HKDH Bhadeshia and CM Wayman. «Phase transformations: nondiffusive». In: *Physical metallurgy*. Elsevier, 2014, pp. 1021–1072 (cit. on p. 10).

[33] E Morosan, HW Zandbergen, BS Dennis, JWG Bos, Y Onose, T Klimczuk, AP Ramirez, NP Ong, and RJ Cava. «Superconductivity in cuxtise2». In: *Nature Physics* 2.8 (2006), pp. 544–550 (cit. on pp. 12, 13).

[34] I Guillamón, H Suderow, S Vieira, Laurent Cario, P Diener, and P Rodiere. «Superconducting density of states and vortex cores of 2H-NbS 2». In: *Physical review letters* 101.16 (2008), p. 166407 (cit. on p. 11).

[35] AH Thompson. «Low temperature magneto-resistance, logarithmic resistivity rise and anisotropic superconductivity in TaS2 (pyridine) 12». In: *Solid State Communications* 13.11 (1973), pp. 1911–1913 (cit. on p. 12).

[36] RA Klemm, A Luther, and MR Beasley. «Theory of the upper critical field in layered superconductors». In: *Physical Review B* 12.3 (1975), p. 877 (cit. on p. 12).

[37] AD McNaught, A Wilkinson, et al. *Compendium of chemical terminology*. Vol. 1669. Blackwell Science Oxford, 1997 (cit. on p. 12).

[38] Y Meng et al. «Protonation-induced discrete superconducting phases in bulk FeSe single crystals». In: *Physical Review B* 105.13 (2022), p. 134506 (cit. on p. 13).

[39] MD Abràmoff, PJ Magalhães, and SJ Ram. «Image processing with ImageJ». In: *Biophotonics international* 11.7 (2004), pp. 36–42 (cit. on p. 16).

[40] *Equi-potential Surface*. URL: `https://www.brainkart.com/article/Equi-potential-Surface_38372/` (cit. on p. 16).

[41] Tadashige Nishikawa and Shunichi Fujimura. «"Beamex ER", new cross-linked polymeric insulated heat-and flame-resistant wires». In: *FAPIG (Tokyo)* (1978), pp. 22–28 (cit. on p. 18).

[42] Go C Dacey and IM Ross. «The field effect transistor». In: *Bell System Technical Journal* 34.6 (1955), pp. 1149–1189 (cit. on p. 19).

[43] K Hayamizu, Y Aihara, H Nakagawa, T Nukuda, and WS Price. «Ionic conduction and ion diffusion in binary room-temperature ionic liquids composed of [emim][BF4] and LiBF4». In: *The Journal of Physical Chemistry B* 108.50 (2004), pp. 19527–19532 (cit. on p. 19).

[44] GC Dacey and IM Ross. «The field effect transistor». In: *Bell System Technical Journal* 34.6 (1955), pp. 1149–1189 (cit. on p. 20).

[45] J Conway and S Watts. *A software engineering approach to LabVIEW*. Prentice Hall Professional, 2003 (cit. on p. 19).

[46] J Bert. *Pulse Tube Cryocoolers: A Cryogen-Free Path To 2K; Department of Physics*. 2007 (cit. on p. 25).

[47] *DISAT*. URL: `https://www.disat.polito.it/` (cit. on p. 24).

[48] AW Van Herwaarden and PM Sarro. «Thermal sensors based on the Seebeck effect». In: *Sensors and Actuators* 10.3-4 (1986), pp. 321–346 (cit. on p. 26).

[49] *HQ graphene*. URL: `http://www.hqgraphene.com` (cit. on p. 32).

[50] *2D semiconductors*. 2008-2022 (cit. on pp. 32–34).

[51] Y Liu, R Ang, WJ Lu, 1WH Song, LJ Li, and YP Sun. «Superconductivity induced by Se-doping in layered charge-density-wave system 1 T-TaS2- x Se x». In: *Applied Physics Letters* 102.19 (2013), p. 192602 (cit. on p. 33).

[52] AH Thompson and BG Silbernagel. «Correlated magnetic and transport properties in the charge-density-wave states of V Se 2». In: *Physical Review B* 19.7 (1979), p. 3420 (cit. on pp. 44, 45).

[53] K Xu, P Chen, X Li, C Wu, Y Guo, J Zhao, X Wu, and Y Xie. «Ultrathin nanosheets of vanadium diselenide: a metallic two-dimensional material with ferromagnetic charge-density-wave behavior». In: *Angewandte Chemie* 125.40 (2013), pp. 10671–10675 (cit. on pp. 45, 46).

[54] N Mott. «Conduction in non-crystalline materials: III. Localized states in a pseudogap and near extremities of conduction and valence bands». In: *Philosophical Magazine* 19.160 (1969), pp. 835–852 (cit. on p. 49).

[55] Alex T Coyle, Robert P Spragg, Prannoy Suraneni, Armen N Amirkhanian, Marisol Tsui-Chang, and William Jason Weiss. «Activation energy of conduction for use in temperature corrections on electrical measurements of concrete». In: *Advances in Civil Engineering Materials* 8.1 (2019), pp. 158–170 (cit. on p. 52).

[56] AP Nayak et al. «Pressure-modulated conductivity, carrier density, and mobility of multilayered tungsten disulfide». In: *ACS nano* 9.9 (2015), pp. 9117–9123 (cit. on pp. 53, 54).

[57] Y Zheng et al. «Controlling phase transition in WSe2 towards ideal n-type transistor». In: *Nano Research* 14.8 (2021), pp. 2703–2710 (cit. on p. 53).

[58] H Arora et al. «Superconductivity in metallic twisted bilayer graphene stabilized by WSe2». In: *Nature* 583.7816 (2020), pp. 379–384 (cit. on pp. 53, 55).

[59] SR Taylor. «Geochim». In: *Cosmochim. Acta* 28 (1964), p. 1273 (cit. on p. 54).

[60] B El-Kareh and LN Hutter. *Fundamentals of semiconductor processing technology*. Springer Science & Business Media, 2012 (cit. on p. 54).

[61] H Li, S Liu, S Huang, Q Zhang, C Li, X Liu, J Meng, and Y Tian. «Metallic impurities induced electronic transport in WSe2: First-principle calculations». In: *Chemical Physics Letters* 658 (2016), pp. 83–87 (cit. on p. 54).

[62] A Azizi, Y Wang, G Stone, A Elias, Z Lin, M Terrones, VH Crespi, and N Alem. «Defect Coupling and Sub-Angstrom Structural Distortions in W1–x Mo x S2 Monolayers». In: *Nano letters* 17.5 (2017), pp. 2802–2808 (cit. on p. 55).

[63] A Prakash and J Appenzeller. «Bandgap extraction and device analysis of ionic liquid gated WSe2 Schottky barrier transistors». In: *Acs Nano* 11.2 (2017), pp. 1626–1632 (cit. on p. 56).

[64] A Sommerfeld. «Zur Elektronentheorie der Metalle». In: *Naturwissenschaften* 16.21 (1928), pp. 374–381 (cit. on p. 60).

[65] M Ettenberg, KL Komarek, and E Miller. «Thermodynamic properties of nickel-tellurium alloys». In: *Journal of Solid State Chemistry* 1.3-4 (1970), pp. 583–592 (cit. on p. 62).

[66] JA Hlevyack et al. «Dimensional crossover and band topology evolution in ultrathin semimetallic NiTe2 films». In: *npj 2D Materials and Applications* 5.1 (2021), pp. 1–9 (cit. on p. 62).

[67] M Putti and G Grasso. «MgB2, a two-gap superconductor for practical applications». In: *MRS bulletin* 36.8 (2011), pp. 608–613 (cit. on p. 62).

[68] M Horio et al. «Two-dimensional type-II Dirac fermions in layered oxides». In: *Nature communications* 9.1 (2018), pp. 1–7 (cit. on p. 63).

[69] SY Tan et al. «Observation of Dirac cone band dispersions in FeSe thin films by photoemission spectroscopy». In: *Physical Review B* 93.10 (2016), p. 104513 (cit. on p. 63).

[70] C Xu et al. «Topological type-II Dirac fermions approaching the Fermi level in a transition metal dichalcogenide NiTe2». In: *Chemistry of materials* 30.14 (2018), pp. 4823–4830 (cit. on p. 63).